

Connecting turbulent velocities and magnetic fields in galaxy cluster simulations with active galactic nuclei jets

K. Ehlert^{1*}, R. Weinberger², C. Pfrommer¹, V. Springel³

¹Leibniz Institute for Astrophysics, An der Sternwarte 16, D-14482 Potsdam, Germany

²Center for Astrophysics | Harvard & Smithsonian, 60 Garden Street, Cambridge, MA 02138, USA

³Max-Planck-Institut für Astrophysik, Karl-Schwarzschild-Str. 1, D-85741 Garching, Germany

Accepted XXX. Received YYY; in original form ZZZ

ABSTRACT

The study of velocity fields of the hot gas in galaxy clusters can help to unravel details of microphysics on small-scales and to decipher the nature of feedback by active galactic nuclei (AGN). Likewise, magnetic fields as traced by Faraday rotation measurements (RMs) inform about their impact on gas dynamics as well as on cosmic ray production and transport. We investigate the inherent relationship between large-scale gas kinematics and magnetic fields through non-radiative magnetohydrodynamical simulations of the creation, evolution and disruption of AGN jet-inflated lobes in an isolated Perseus-like galaxy cluster, with and without pre-existing turbulence. In particular, we connect cluster velocity measurements with mock RM maps to highlight their underlying physical connection, which opens up the possibility of comparing turbulence levels in two different observables. For single jet outbursts, we find only a local impact on the velocity field, i.e. the associated increase in velocity dispersion is not volume-filling. Furthermore, in a setup with pre-existing turbulence, this increase in velocity dispersion is largely hidden. We use mock X-ray observations to show that at arcmin resolution, the velocity dispersion is therefore dominated by existing large-scale turbulence and is only minimally altered by the presence of a jet. For the velocity structure of central gas uplifted by buoyantly rising lobes, we find fast, coherent outflows with low velocity dispersion. Our results highlight that projected velocity distributions show complex structures which pose challenges for the interpretation of observations.

Key words: methods: numerical – galaxies: clusters: intracluster medium – MHD – cosmic rays – galaxies: jets – galaxies: active

1 INTRODUCTION

Roughly half of all known galaxy clusters show cooling times $\lesssim 1$ Gyr but lack the expected high star formation and cooling rates (Fabian 2012). Active galactic nuclei (AGN) powered by supermassive black holes (SMBH) in the center of these cool-core (CC) clusters inflate buoyantly rising bubbles of hot gas, which are believed to heat the intra-cluster medium (ICM) (Gitti et al. 2012; McNamara & Nulsen 2012). The details of the heating process are unknown. Possible mechanisms include mixing of hot bubble gas with the ICM (Yang & Reynolds 2016; Hillel & Soker 2017b, 2018), possibly facilitated by external cluster turbulence (Bourne et al. 2019; Bourne & Sijacki 2020), the decay of turbulence (Zhuravleva et al. 2014, 2018; Fujita et al. 2020; Mohapatra & Sharma 2019), the uplift of cold gas in the wake of bubbles (Guo et al. 2018; Chen et al. 2019), the dissipation of sound waves (Fabian et al.

2017; Tang & Churazov 2017; Bambic & Reynolds 2019), the dissipation of weak shocks (Li et al. 2017; Martizzi et al. 2019) or the damping of cosmic ray (CR) induced Alfvén waves (Loewenstein et al. 1991; Guo & Oh 2008; Enßlin et al. 2011; Pfrommer 2013; Jacob & Pfrommer 2017a,b; Ruszkowski et al. 2017). The structure of the velocity field in the ICM contains important information about the relevance of many of these processes: the amplitude and scale of the ICM turbulence can be used to infer a turbulent dissipation rate (Zhuravleva et al. 2014), turbulent velocities combined with the cooling time set an effective range for turbulent transport (Fabian et al. 2017) and the morphology of the magnetic and velocity field impacts the transport of CRs (Ehlert et al. 2018).

Observationally, many details of the velocity structure of the hot gas in the ICM remain open questions (Simionescu et al. 2019). Early results of the *Suzaku* satellite found no velocity gradient within their calibration uncertainty, which provided upper limits of a few thousand km s⁻¹ for cluster bulk velocities (e.g., Ota et al. 2007; Ota & Yoshida 2016; Sugawara et al. 2009; Tamura et al. 2011, 2014). Spectral analysis of *XMM-Newton* data put first di-

* E-mail: kehlert@aip.de

rect constraints on the turbulent motions in the ICM, finding large scale velocities on the order of hundreds of km s^{-1} (Sanders et al. 2010; Bulbul et al. 2012; Sanders & Fabian 2013; Pinto et al. 2015). Resonant scattering of lines in the core of clusters causes an apparent suppression of some lines compared to others. Thus, turbulent velocities can be constrained due to their influence on the optical depth (see Gu et al. 2018, for a review).

Recent more refined analysis of resonant scattering with *XMM-Newton* RGS spectra found turbulent velocities in the center of clusters on scales $\lesssim 10$ kpc of hundreds of km s^{-1} (e.g., Xu et al. 2002; Werner et al. 2009; De Plaa et al. 2012; Ogorzalek et al. 2017). A different inference method relies on X-ray fluctuations in the smooth cluster potential that correlate with the velocity fluctuations (Schuecker et al. 2004; Churazov et al. 2012; Gaspari & Churazov 2013). The method allows the computation of the velocity power spectrum, which provides constraints on the kinematic viscosity in clusters. In agreement with discussed alternative methods, recovered velocities of gas motions in the center of analyzed clusters reach a few hundred km s^{-1} (Walker et al. 2015; Zhuravleva et al. 2018). Most recently, the significant increase in spectral resolution and high broadband spectral resolution allowed the X-ray satellite *Hitomi* to directly determine the bulk velocities of Perseus to be $|v_{\text{bulk}}| \lesssim 100 \text{ km s}^{-1}$ and turbulent velocities of $\sigma_{\text{los}} \approx 100 - 200 \text{ km s}^{-1}$ on spatial scales of ≈ 20 kpc (Hitomi Collaboration 2016, 2018). However, detailed high-resolution velocity maps of clusters are not available and the impact of the AGN on the velocity remain unclear, which is crucial for identifying relevant heating mechanisms.

However, we can make progress by realizing that magnetic fields are tightly coupled to fluid velocities which can amplify seed magnetic fields that can themselves back-react to the flow velocities provided they are sufficiently strong. This coupling may potentially allow velocities to be deduced from magnetic fields and vice versa. And with that it provides the basis for this paper. In the framework of numerical ideal MHD, a turbulent velocity field leads to the amplification of the magnetic field \mathbf{B} , with the rate of change given by the induction equation,

$$\frac{\partial \mathbf{B}}{\partial t} = -\mathbf{v} \cdot \nabla \mathbf{B} + \mathbf{B} \cdot \nabla \mathbf{v} - \mathbf{B} \nabla \cdot \mathbf{v} + \eta \nabla^2 \mathbf{B}, \quad (1)$$

which relates magnetic field evolution to the velocity field \mathbf{v} and the magnetic diffusivity η . Here and elsewhere in the paper we adopt the Gaussian cgs system of units and η denotes the magnetic diffusivity, which has units of a diffusion coefficient. The evolution is governed by advection, stretching, compression and (numerical) dissipation of the field, respectively.

The induction equation provides the theoretical basis for a turbulent dynamo that amplifies a seed magnetic field (e.g., Kazantsev 1968; Subramanian 1999; Schober et al. 2015; Beresnyak & Miniati 2016; Schekochihin & Cowley 2006). Numerical simulations support this picture (Dolag et al. 2005; Ryu et al. 2008; Beresnyak 2012; Cho 2014; Roh et al. 2019). The dynamo reaches magnetic-to-thermal pressure ratios of a few percent (Schober et al. 2015; Vazza et al. 2018). Additional amplification is expected via compression, shocks and CRs (see review by Donnert et al. 2018). AGN feedback may cause advection of galactic magnetic fields to the ICM (Dubois et al. 2009; Xu et al. 2009; Donnert et al. 2009).

The evolution of the velocity field, in turn, is given by

$$\frac{\partial \mathbf{v}}{\partial t} = -\mathbf{v} \cdot \nabla \mathbf{v} - \frac{\nabla p}{\rho} - \nabla \Phi + \frac{1}{4\pi\rho} \left[\mathbf{B} \cdot \nabla \mathbf{B} - \frac{1}{2} \nabla \cdot (\mathbf{B}^2) \right], \quad (2)$$

where p denotes the thermal pressure, ρ is the gas mass density, and Φ is the (external) gravitational potential. The terms on the right describe advection, pressure force, gravity, magnetic tension and magnetic pressure, respectively. These equations, combined with the fact that the dynamical timescale is smaller than the lifetime of galaxy clusters, imply that intra-cluster medium turbulence is expected to show both, turbulent velocities as well as magnetic fields of corresponding specific energy. For reference, equipartition of kinetic and magnetic energy density implies

$$\frac{\rho}{10^{-25} \text{ g cm}^{-3}} \left(\frac{|\mathbf{v}|}{100 \text{ km s}^{-1}} \right)^2 \approx \left(\frac{|\mathbf{B}|}{11.2 \mu\text{G}} \right)^2. \quad (3)$$

Indeed, observations of large-scale diffuse radio structures on up to Mpc scale in galaxy clusters, i.e. radio halos, support the notion that the ICM is magnetized (see review by van Weeren et al. 2019). Faraday RMs uncover the strength and scale of magnetic turbulence in clusters (Clarke 2004). Assuming that the magnetic field scales as a power-law with density, the expected RM from simulated fields can be compared to observations to measure its strength and injection scale. Applying this method to radio galaxies in the Coma cluster, Bonafede et al. (2010) determine a central magnetic field strength of $5 \mu\text{G}$. Additionally, Kuchar & Enßlin (2011) analyzed the magnetic field of Hydra A and found a central magnetic field strength of $36 \mu\text{G}$. Generally, hotter, more massive clusters show larger dispersion in RM distributions (Govoni et al. 2010) and magnetic power spectra are consistent with a Kolmogorov slope (e.g., Vogt & Enßlin 2005; Guidetti et al. 2008; Vacca et al. 2012; Govoni et al. 2017).

This paper aims to shed light on the connection between large-scale magnetic and velocity fields and their observables, i.e. Faraday RM and X-ray emission-line broadening, by studying simulations of decaying cluster turbulence. Simulating an AGN outburst in a Perseus-like cluster, we demonstrate that jet driven turbulence is mostly limited to the near vicinity of the jet, more specifically to the wake of the bubbles. We also relate the kinetic to the Faraday RM powerspectra and detail the velocity fields of dragged up material by the jet.

For this, we describe our initial conditions and simulation setup in Section 2. In Section 3, we analyze our simulations of the ICM without jets. In Section 4, we then study the effects of AGN driven turbulence in simulations with and without pre-existing turbulence, and connect them to X-ray and RM maps. Subsequently, in Section 5, we focus on AGN jet induced uplifts and conclude in Section 6.

2 METHODS

We use simulations of isolated galaxy clusters to study the impact of AGN driven jets on the magnetized ICM. The equations of ideal magnetohydrodynamics (MHD) are solved on a moving mesh using the AREPO code (Springel 2010; Pakmor et al. 2016a). CRs created in the jets are treated as a second fluid including advection, Alfvénic, hadronic and leptonic losses (Pfrommer et al. 2017) and anisotropic diffusion along magnetic field lines (Pakmor et al. 2016b). The simulation setup closely resembles the one in previous work (Ehlert et al. 2018), with some minor changes.

2.1 Initial conditions

We model our simulated cluster after the Perseus cluster: the dark matter profile follows a Navarro-Frenk-White (NFW) profile

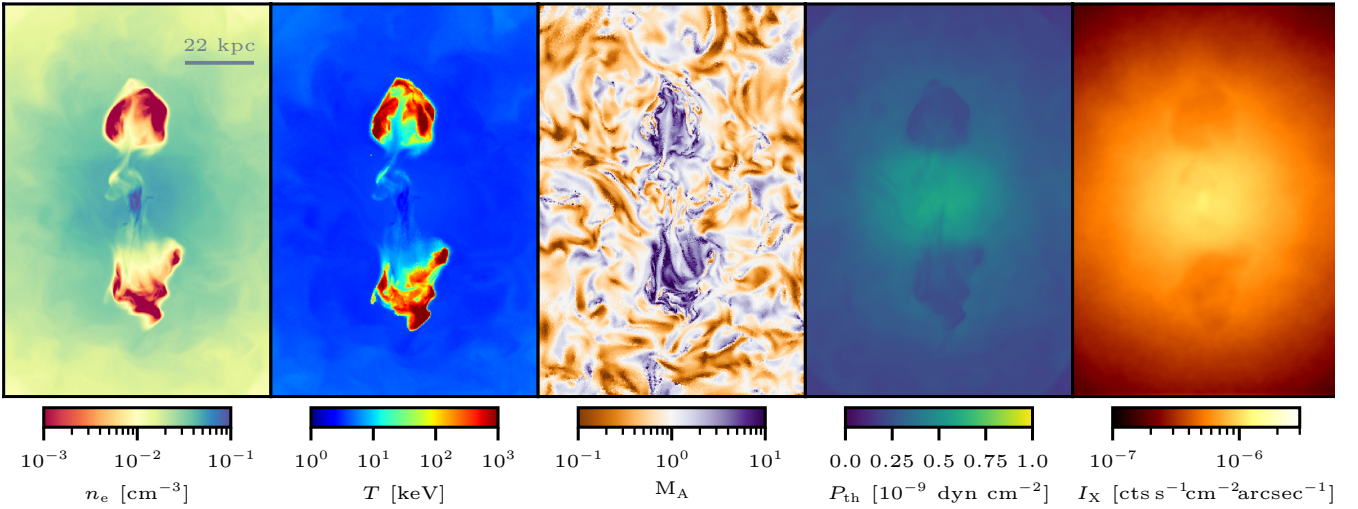


Figure 1. We show thin projections ($132 \text{ kpc} \times 90 \text{ kpc} \times 4 \text{ kpc}$) of density ρ , temperature T , Alfvénic Machnumber $M_A = \sqrt{\epsilon_{\text{kin}}/\epsilon_B}$, thermal pressure P_{th} and 2 – 12 keV X-ray surface brightness I_X centred on the BH. To reduce photon noise, the simulated X-ray exposure is 2.5 Ms and the map has been smoothed with a Gaussian kernel of 2 arcsec width. The bubbles are in the process of disruption by dense central gas that is accelerated upwards in the wake of the bubbles.

(Navarro et al. 1996, 1997) with virial radius¹ $R_{200,c} = 2.12 \text{ Mpc}$, virial mass $M_{200,c} = 8 \times 10^{14} M_{\odot}$ (Reiprich & Bohringer 2002), and concentration parameter $c_{\text{NFW}} = 5$. We adopt the electron number density profile from Churazov et al. (2003) rescaled to a cosmology with $h = 0.67$:

$$n_e = 46 \times 10^{-3} \left[1 + \left(\frac{r}{60 \text{ kpc}} \right)^2 \right]^{-1.8} \text{ cm}^{-3} + 4.7 \times 10^{-3} \left[1 + \left(\frac{r}{210 \text{ kpc}} \right)^2 \right]^{-0.87} \text{ cm}^{-3}. \quad (4)$$

We include a turbulent magnetic field in the ICM. In Fourier space the magnetic field follows a Kolmogorov spectrum on scales smaller than the injection scale $k_{\text{inj}}^{-1} = 37.5 \text{ kpc}$ and white noise on larger scales. Our choice of k_{inj}^{-1} is motivated by observations of RMs of CC clusters, which find magnetic fields fluctuating on scales from a few to tens of kpc (Vacca et al. 2018). Motivated by Bonafede et al. (2010), who find their large sample of RMs for Coma to be consistent with a constant magnetic-to-thermal pressure ratio, we scale the concentric shell averaged magnetic field strength to a magnetic-to-thermal pressure ratio of $X_{B,\text{ICM}} = 0.05$, independent of radius. The strength of the magnetic field is motivated by radio synchrotron (de Gasperin et al. 2012) and RMs (Kuchar & EnBlin 2011) by scaling magnetic field strength to the density of the Perseus cluster (see Section 3.1 in Pfrommer 2013). We refer to our previous work (Ehlert et al. 2018) for the precise procedure to set up this divergence-free field.

2.2 Jet modeling

The launching of the jet follows previous work (Weinberger et al. 2017; Ehlert et al. 2018), with some minor modifications: we set up two spherical injection regions with radius $r_j = 1.65 \text{ kpc}$ at a

distance of 3.3 kpc on opposite sides of a central SMBH. These regions serve as inflow boundary regions, in which the jet density $\rho_{\text{jet}} = 10^{-28} \text{ g cm}^{-3}$ is kept constant throughout the injection and the thermal energy, as well as a weak toroidal magnetic field with relative energy density $X_{B,\text{jet}} = 0.1$ are adjusted to be in pressure equilibrium with the surrounding medium. To ensure overall mass conservation, the mass that was taken out of (or put into) the injection region is added (or removed) from the SMBH surroundings that is not within these injection regions. After accounting for the (comparably small amount of) energy required for the preparation of this state, the remaining energy is added in the form of kinetic energy creating bipolar outflows from the jet regions.

In our previous work, we assumed a jet opening angle of zero. The velocity gradient along the jet axis requires a minimum number of ~ 10 cells to be resolved. With increasing resolution, the momentum is distributed over a smaller volume and the jet speed increases. As a result, a given amount of injected energy produced lobes at larger cluster-centric distances than observed, especially for highly resolved jets. This may hint towards a more complex small scale jet physics below the resolution limit of our simulation². To cure this short-coming, here we introduce a jet opening angle, such that momentum changes are not strictly bi-directional. We determine the cone with a 30-degree half-opening angle that encloses one of the spherical injection regions and has its tip centered on the SMBH. The position vector of a cell relative to the tip of this cone is used as the direction in which the momentum is injected. We note that due to geometrical effects and the larger weighting of central cells, 30 degree represents the largest possible angle from the jet axis that the momentum kick can be applied, while half of the momentum is injected at angles < 10 degrees from the jet axis.

This opening angle leads to an earlier termination of the jet, producing lobes at smaller distances from the galaxy cluster center,

¹ We define the cluster virial radius as the radius at which the mean enclosed density equals 200 times the critical density of the universe today.

² Possible effects could include the interaction with a clumpy interstellar medium (Mukherjee et al. 2016), jet instabilities such as the magnetic kink instability (Tchekhovskoy & Bromberg 2016; Mukherjee et al. 2020) or an actual, wider opening angle wind component (Yuan et al. 2015).

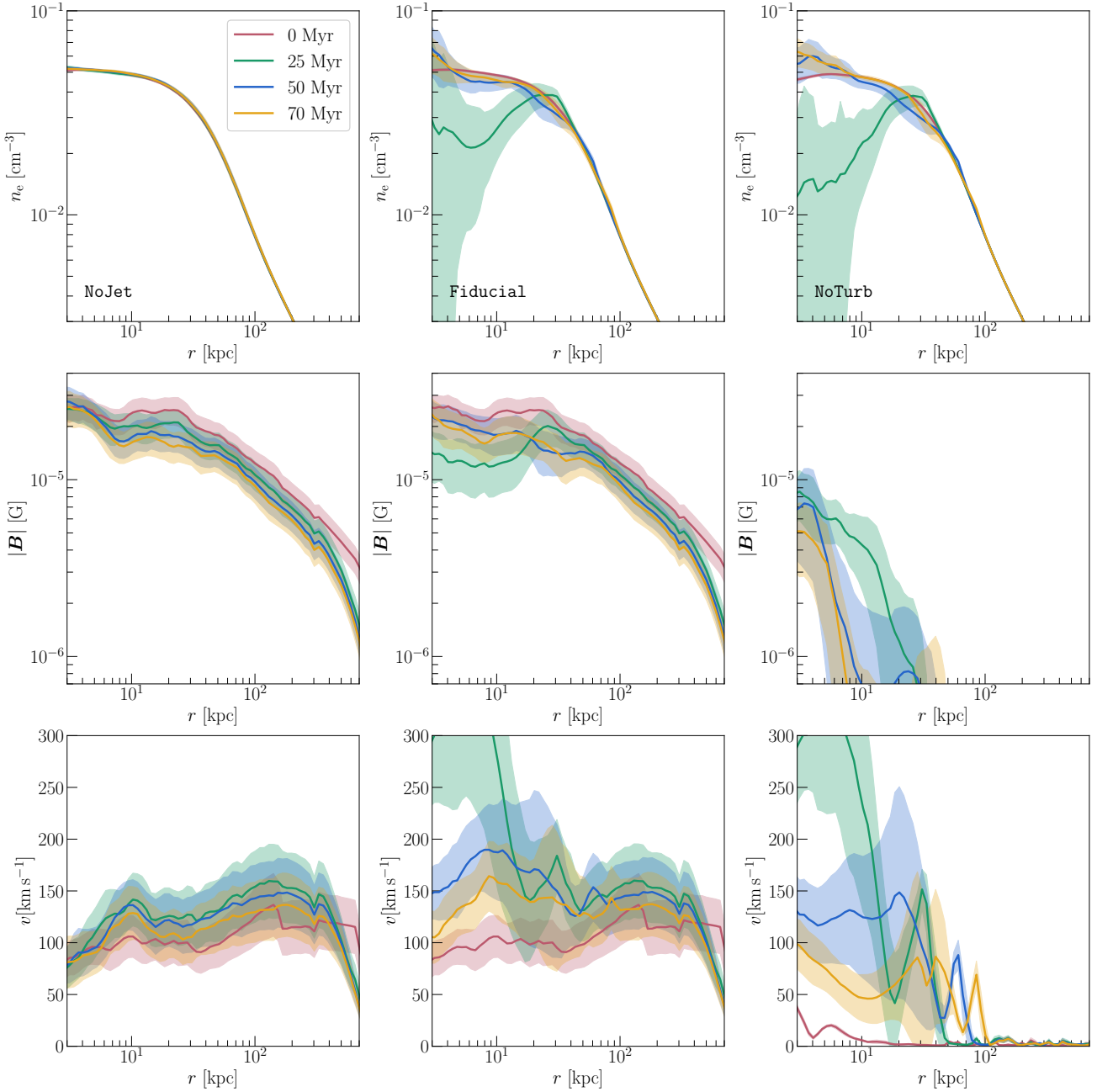


Figure 2. From top to bottom we show radial profiles of volume-weighted density, square root of volume-weighted magnetic field strength and square root of mass-weighted velocities for models `NoJet`, `Fiducial` and `NoTurb` (from left to right) at stated times. The bubbles are visible as depressions at $r < 20$ kpc at 25 Myr. The turbulent magnetic field decays as a function of time. AGN-induced velocities are limited to the vicinity of the bubble.

in rough agreement with observations in the Perseus cluster (discussed in Section 4.1). Figure 1 shows a snapshot of such a simulation including thin density and temperature slices, 25 Myr after the jet became inactive after it was on for the same time.

Since we cannot model the acceleration of CR protons self-consistently within this model, we include it in our lobes by converting thermal to CR energy until the desired CR-to-thermal energy ratio $X_{\text{cr,acc}} = 1$ is obtained while the jet is active. We magnetically isolate the injection region to inhibit unphysical diffusion of CRs. In the ICM, CRs are expected to scatter on self-generated Alfvén waves (Kulsrud 2005). Due to inefficient Alfvén wave damping CRs are confined to stream down their pressure gra-

dient ∇P_{cr} close to the Alfvén speed v_A (Zweibel 2013; Thomas & Pfrommer 2019; Thomas et al. 2020). CRs that stream faster than the local Alfvén speed excite the streaming instability that continuously generates Alfvén waves, which experience damping processes. Thereby, CR energy is effectively transformed into thermal energy via *Alfvén heating* with power $H_{\text{cr}} = |v_A \cdot \nabla P_{\text{cr}}|$. In line with Sharma et al. (2009) and Wiener et al. (2017), we introduce an effective CR diffusion coefficient $\kappa_{\text{cr,A}} = 10^{29} \text{ cm}^2 \text{ s}^{-1}$ and emulate CR streaming by including CR advection, anisotropic diffusion and account for Alfvénic losses (see Ehlert et al. 2018, for more details).

We summarize adopted parameters for our simulations in Ta-

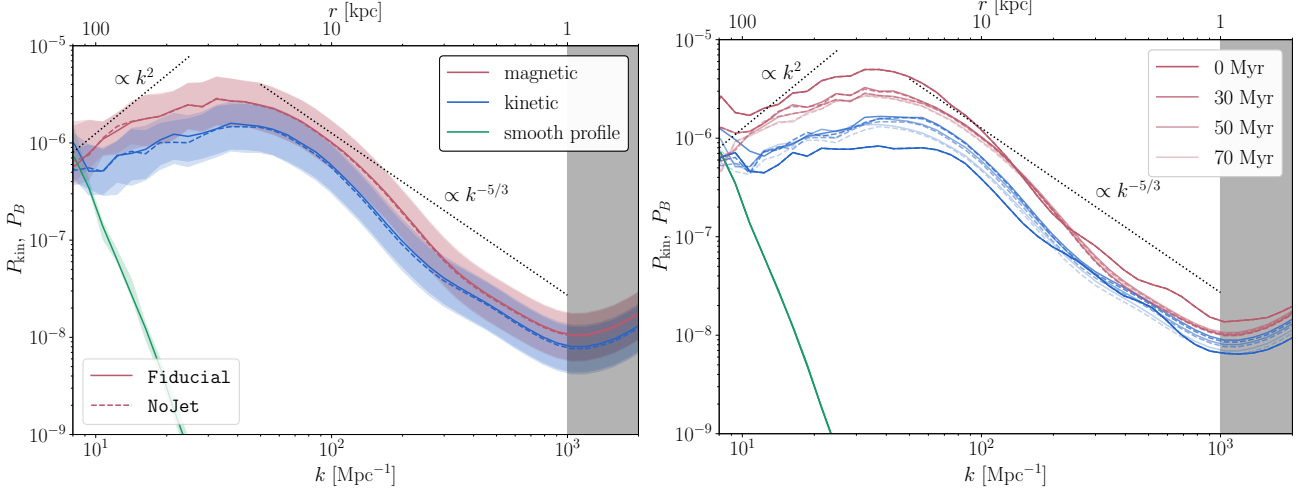


Figure 3. We show one-dimensional power spectra of kinetic energy density, magnetic energy density (left panel) and its evolution at 0, 30, 50, 70 Myr (right panel) of a BH-centred box with $L = 400$ kpc of Fiducial (lines) and NoJet (dashed). Additionally, power spectra assuming a smooth magnetic profile are plotted (‘smooth profile’) to quantify the contributions from the cluster profile, which only become relevant on large scales (> 200 kpc). Shaded regions show an artificial increase in power due to leaking from higher scales which is caused by the inherent (and incorrect) assumption of periodicity. The influence of the AGN on the power spectrum is minuscule. Magnetic tension initially leads to an increase of kinetic power. After 30 Myr the driving by the progressively more relaxed magnetic field (as evident by decaying magnetic power) cannot keep up with the competing decay of kinetic turbulence. This leads to an overall decrease of kinetic power.

Jet parameters		
Jet power	P_{jet}	$10^{45} \text{ erg s}^{-1}$
Jet life time	τ_{jet}	15 Myr
Jet density	ρ_{target}	$10^{-28} \text{ g cm}^{-3}$
Jet launching region	r_{j}	1.65 kpc
CR acceleration	$X_{\text{cr,acc}}$	1
Jet magnetization	$X_{B,\text{jet}}$	0.1
Magnetic field parameters		
Injection scale	k_{inj}	$37.5^{-1} \text{ kpc}^{-1}$
Resolution		
Target mass	$m_{\text{target},0}$	low res.: $1.5 \times 10^7 M_{\odot}$ interm. res.: $1.5 \times 10^6 M_{\odot}$ high res.: $4.5 \times 10^4 M_{\odot}$
Jet target volume	$V_{\text{target}}^{1/3}$	lower res.: 873 pc interm. res.: 405 pc high res.: 188 pc
Minimum volume	V_{min}	$V_{\text{target}}/2$

Table 1. Parameters for jet, the magnetic field and refinement.

ble 1 and list the main simulations in Table 2. For the high resolution runs, to focus the computational resources on the region of interest, we chose the target mass to be dependent on distance from the centre r ,

$$m_{\text{target},0} = 3 \times 10^4 M_{\odot} \exp(r/100 \text{ kpc}), \quad (5)$$

with cells at the outskirts limited to a maximum volume. In the following we focus our analysis on our high resolution simulations unless stated otherwise.

Label	Jet active	$X_{B,\text{ICM}}$	Resolution
Fiducial	True	0.05	High
NoTurb	True	0	High
NoJet	False	0.05	High
X25	True	0.25	Interm.
X5	True	0.05	Interm.
X1	True	0.01	Interm.

Table 2. List of simulations and magnetic parameter variations. Note, run NoTurb is setup without magnetic fields in a hydrostatic atmosphere.

2.3 Analysis

2.3.1 X-ray emission

To create velocity dispersion maps, we create synthetic X-ray observations of the simulation snapshots and fit the line profile of the mock spectrum. In particular, we employ the PYXSIM code (ZuHone & Hallman 2016) using the specific internal energy and density of each gas cell, assuming a metallicity of the gas to be 0.7 solar metallicity and Asplund et al. (2009) element abundance ratios. The code makes use of the APEC library (Smith et al. 2001, version 3.0.9) to calculate emission spectra in the energy range 2 – 12 keV. The spectra are sampled with photon packages, taking into account thermal and Doppler broadening. The photon packages are then projected onto the detector plane, taking into account ISM absorption using the Tuebingen-Boulder absorption model (Wilms et al. 2000) assuming a column density of $4 \times 10^{-20} \text{ cm}^{-2}$, and astrophysical backgrounds are added. We put the galaxy cluster at a redshift of $z = 0.017284$, with 1 arcmin corresponding to 21 kpc using the cosmological parameters $h = 0.67$, $\Omega_m = 0.3$, $\Omega_{\Lambda} = 0.7$. We then convolve the photons with instrumental effects of XRISM Resolve using the SOXS library, including an Auxiliary Response File (ARF), point spread function (PSF) effects as well as energy scattering is introduced using a Redistribution Matrix File

(RMF)³, and perform the synthetic observation with exposure time 250 ks.

We then use the mock spectrum and fit a multi-Gaussian to the FeXXV He- α complex. Similar to [Hitomi Collaboration \(2016\)](#), we use a single width for all but the strongest line, as well as a single offset, but variable amplitudes, thus ending up with 12 fit-parameters. Note however that we omit the fitting of the weaker lines for simplicity. We obtain the bulk velocity and line width from the fit parameters. Subtracting the square of the expected thermal broadening (assuming a single-temperature gas at 4 keV) from the squared line width, we obtain the squared velocity dispersion.

To assess the effect of the different steps in this pipeline, we also produce (2 – 12 keV) emission weighted velocity dispersion maps as well as maps of ‘ideal’ observations (omitting instrumental effects). We discuss these effects in [Appendix C](#). Note, however, that due to the idealized nature of the simulations, uncertainties resulting from temperature and metallicity variations are not captured in this setup.

2.3.2 Faraday rotation measure

The rotation measure RM is given by

$$\text{RM} = \frac{e^3}{2\pi m_e^2 c^4} \int_0^{s_e} ds n_e B, \quad (6)$$

where the magnetic field is integrated along the line of sight from the source at s_e to the observer at $s = 0$.

This is done by sampling the magnetic and electron density field with a finely spaced ($\Delta x = 90$ pc) 3D cartesian grid of dimensions 110 kpc – 70 kpc – 1.5 Mpc, and numerically integrating along the third axis for each pixel.

2.3.3 Kinematics of uplifted gas

In order to study the motions of the central ICM induced by the AGN, we initialize a passive scalar within 5 kpc of the SMBH to unity. This scalar is only advected with the flow and prone to dilution. To determine the velocity dispersion and mean velocity in individual pixels in the projected map we compute scalar mass weighted histograms. For this, we only consider cells with mass fractions of $> 10^{-3}$. Velocity dispersion and mean velocity correspond to the variance and mean of a Gaussian that we fit to the highest peak in the velocity distribution. If fitting errors exceed 50%, we double the bin size in the corresponding pixel, refit the velocity distribution, and check new fitting errors. This retains a few pixels mostly at the outskirts. We confirmed that our results remain invariant under variations of detailed parameters (bin size, mass fraction, etc.). All individual fits contain of order 10^4 unique data points. Thereby, sufficient sampling is ensured by enforcing high resolution in the ICM.

3 LARGE-SCALE TURBULENCE

To study the impact of AGN driven jets on ICM turbulence, we first discuss the evolution of the ICM in absence of jets as well as the lobe properties. Subsequently, we discuss the impact of jets in both, a quiescent and a turbulent ICM environment in [Section 4](#).

First, we focus on the inherent link between equations (1) and (2) which allows us to resort to the case of decaying MHD turbulence. Since the ICM is in hydrostatic equilibrium, i.e. the total pressure gradient is balanced by gravity, magnetic tension forces convert magnetic energy to kinetic energy as described in equation (2). Note that in this setup the magnetic field initially dominates over the kinetic turbulence. This implies that the magnetic field is not substantially replenished by dynamo processes and thus magnetic energy decreases over time, while the kinetic energy increases initially. This can be seen in the radial profiles of electron number density n_e , magnetic field strength $|\mathbf{B}|$ and absolute velocity v at different times as shown in [Figure 2](#). The magnetic field strength decreases independently of radius by ≈ 0.2 dex after 70 Myr. After ≈ 30 Myr, stirring by magnetic tension forces becomes subdominant compared to turbulent dissipation, leading to a decrease in kinetic energy.

To study the scale-dependence of magnetic and kinetic energy density, we show the respective one-dimensional power spectra in [Figure 3](#). The magnetic power decays on most scales as shown in the right panel. To quantify the modulation of the spectrum by the profile of the cluster, we plot the power spectrum of a smooth magnetic field with magnetic-to-thermal pressure ratio $X_{B,ICM}$. Magnetic tension stirs the medium and thereby increases the kinetic power. Similarly, kinetic turbulence decreases on all scales after 30 Myr. The modulation due to the profile of the cluster dominates the large scales of the power spectra ($k \lesssim (100 \text{ kpc})^{-1}$). On scales $(100 \text{ kpc})^{-1} \gtrsim k \gtrsim (40 \text{ kpc})^{-1}$, the magnetic field roughly follows a white noise distribution. On smaller scales a Kolmogorov slope is observed.

Having established the overall behaviour, we now show synthetic observables of our simulations after 50 Myr when both magnetic and kinetic fields decay globally. In [Figure 4](#), we show (from top to bottom) slices of the velocity, the velocity dispersion along the line of sight, slices of the magnetic field and the RM of NoJet, Fiducial and NoTurb (from left to right) at 50 Myr.

We find Faraday RMs that are an order of magnitude above observed values. This is somewhat surprising as magnetic field parameters were directly taken from observations. The magnetic field of the jet has negligible effect on the overall RM (see [Section A](#)). We identify four effects that could be responsible for the discrepancy. (i) Possibly our adopted coherence scale is too large and we therefore underpredict depolarization. To test this hypothesis, we ran an additional simulation with an injection scale of $k_{inj} = 15^{-1} \text{ kpc}^{-1}$, which decreases RM by 30% (see [Figure 5](#)). (ii) Observed RMs are limited to few small patches in clusters that are provided by the angular extends of radio lobes. Especially the bright central radio sources in CC clusters imply a large dynamic range that challenges high-frequency polarized observations of lobes, which are negligibly affected by Faraday depolarisation. (iii) Beam smoothing artificially lowers the dispersion of observed RMs. We neglect this effect here. (iv) [Vazza et al. \(2018\)](#) find their simulated magnetic fields to depart from a Gaussian distribution that is usually assumed when modeling Faraday RMs. Consequently, observations of RM possibly overestimate cluster magnetic field strengths. This highlights the relevance of cosmological MHD simulations that are able to self-consistently drive and sustain large scale magnetic fields. Moreover, this calls for a dedicated synthetic modeling of observations to take into account all possible observational effects.

The velocity dispersion σ_{los} corresponds to the variance of a Gaussian fit to X-ray weighted velocities along the line of sight. Gas velocities $|v|$ in the ICM reach a few hundred km/s through-

³ We use the ARF and PSF file version 20170818.

out the cluster in simulations with initial turbulent magnetic field (Fiducial and NoJet). These translate to a velocity dispersion of $\sigma_{\text{los}} \sim 100 \text{ km s}^{-1}$ (second row; left and central panel), which corresponds to the observed levels by *Hitomi*. This gives us another indication that our assumed field strengths are too high as this magnitude of velocity dispersion would hardly be able to sustain our initial field strengths. Varying magnetic field strengths, we find that velocity dispersion induced by fields with weaker field strengths ($\times 1$) yield a velocity dispersion of $\approx 30 - 60 \text{ km s}^{-1}$ (Figure A1). Higher field strengths ($\times 25$) yield a velocity dispersion of $\approx 130 - 180 \text{ km s}^{-1}$ (see Appendix A). We confirmed the numerical convergence of these results (Figure A2).

Thereby, the magnetic field strength in combination with the turbulent injection scale directly corresponds to a range in velocity dispersion at generally observed levels. Detailed simulations of cluster evolution therefore provide a direct link between magnetic field strength and tracers of velocity. Fundamentally, this demonstrates that RM and line broadening in X-ray spectra are just two sides of the same coin with their physical origin in cluster turbulence. The presence of magnetic turbulence implies velocity dispersion and vice versa. Our simulations of decaying turbulence are meant as a proof of concept to explore the relationship between velocity fields and magnetic fields. In reality, perturbations to the cluster potential induced by merger or accretion induce velocity fluctuations that excite a small-scale dynamo, which leads to exponential amplification of the magnetic field on the dissipation scale. After equilibrating with the kinetic energy at this scale the magnetic field might inverse cascade and is expected to saturate at a fraction of the kinetic energy (e.g., Schober et al. 2015; Dominguez-Fernandez et al. 2019), unlike what we have adopted in the initial conditions. Our results highlight the necessity for a self-consistent turbulent dynamo to amplify the magnetic field to equilibrium levels to reliably determine the normalization in the relationship between RM and ICM velocity dispersion. We conclude that one can predict levels of turbulence and magnetic field strengths by observing the other, provided the turbulent injection scale and the growth history is correctly simulated.

4 IMPACT OF JETS ON THE ICM

4.1 Lobe properties

In Figure 1, we show the bubble after 50 Myr, i.e. 25 Myr after the jet became inactive. From left to right, we show density, temperature, Alfvénic Mach number, thermal pressure and X-ray emissivity. The bubbles appear as cavities in the integrated X-ray emissivity. The Alfvénic Mach number corresponds to the ratio of kinetic and magnetic energy density, which, in parts of the ICM reaches $M_A < 1$. Thus the magnetic pressure is dominant and stirs the medium. The jet inflated lobes that rise buoyantly in the cluster atmosphere. At this time, the Rayleigh-Taylor instability starts to markedly disrupt the bubbles. In the wake of the bubbles dense gas is pulled upwards from below. The core of both bubbles is already filled with denser ICM and the southern bubble is in the process of splitting (see density and temperature map). The thermalization of kinetic energy during jet propagation and lobe formation drastically lowers the magnetic-to-thermal pressure ratio compared to the initial value in the jet, $X_{B,\text{jet}}$. Consequently, the magnetic field becomes subdominant in the lobes (see Alfvénic Mach number $M_A > 1$). In the thermal pressure map the bubbles appear as cavities due to the significant pressure support by CRs, as is evident from the large CR-to-thermal pressure ratio $X_{\text{cr}} \geq 0.5$.

The total work required to inflate the lobes can be quantified as the sum of $p_{\text{tot}}V$ of all cells with a jet scalar contribution $X > 10^{-3}$ (assuming that the bubbles are in pressure equilibrium with the ambient ICM). Here $p_{\text{tot},i}$ is the total pressure of cell i , taking into account thermal, CR and magnetic pressure and V its volume. In the present snapshot the energy determined this way is $\sum_i p_{\text{tot},i} V_i = 9.9 \times 10^{58} \text{ erg}$ for both lobes combined. The energy estimate changes by roughly 30% if the threshold for X is changed by an order of magnitude, highlighting the robustness of this result.

The thermal, CR and magnetic energies in the lobe are $1.1 \times 10^{59} \text{ erg}$, $7.6 \times 10^{58} \text{ erg}$ and $7.2 \times 10^{56} \text{ erg}$, respectively, constituting a total lobe enthalpy of $2.8 \times 10^{59} \text{ erg} = 2.87 \sum_i p_{\text{tot},i} V_i$ (the total injected energy is 4.7×10^{59}). We note that CR and thermal energy in the active jet are brought to equipartition by construction, implying an enthalpy of $3 \sum_i p_{\text{tot},i} V_i$ at these times. The subsequent dominance of the thermal component is due to CRs diffusing out of the lobe during the 35 Myr since the termination of the jet. Adiabatic expansion of the lobe drives the lobe towards being more CR dominated (since the adiabatic index of the CR fluid is lower). However, this effect is evidently smaller than diffusive CR losses. We can also infer that about 60 per cent of the injected jet energy is no longer associated with the lobes. This energy has been (i) dissipated in the bow shock during jet propagation, (ii) invested in pdV work on the ambient ICM during the formation and expansion of the lobes, and (iii) lost by diffusing CRs that have escaped the lobes as well as hydrodynamic mixing of lobe material with the surroundings.

The extent and shape of the lobes can be evaluated from the X-ray emissivity image, with a lobe diameter of about 20 kpc at a distance of 25 kpc from the center. These values can be compared to literature values of the lobes in the Perseus Cluster, e.g. Birzan et al. (2004); Rafferty et al. (2006); Diehl et al. (2008), which have similar dimensions and positions. We are therefore confident that the behaviour of these lobes is similar enough to meaningfully compare their effect in the simulated ICM to observational data.

4.2 Dynamical impact of jets

Having presented the properties of the ICM and the lobes, we move on to focus on the effect of a single jet outburst on observable ICM properties.

The inflation of the bubble is visible as a drop in both density and magnetic field strength within the inner 10 kpc at 25 Myr in Figure 2. The compression of the upstream gas due to the shock front is also evident in the profile shown in Figure 2. From the magnetic field and particularly the absolute velocity profiles, it becomes evident that the jet does have some impact on the kinematic structure of the gas within the range of the lobe itself, however not beyond this radius. The simulations without initial turbulence clearly show the limited range of the turbulent driving of the AGN lobes.

Turning to the spatial distribution of the turbulence using line of sight velocity and velocity dispersion in Figure 4, it becomes evident that the arcmin spatial resolution mostly reveals large-scale turbulence which in our simulations originates from the initial conditions, rather than the jet. However, a small, but subdominant effect from the jet is observable, yet only differentially. In the case of a quiescent ICM it becomes particularly clear that the impact on the ICM turbulence is only present at the location of the lobes and in their past trajectory, disfavoring the idea that the lobes can sustain ICM turbulence throughout the entire cluster core and on scales up to several tens of kpc. This also suggests that the observations probing these spatial scales might not directly probe AGN induced

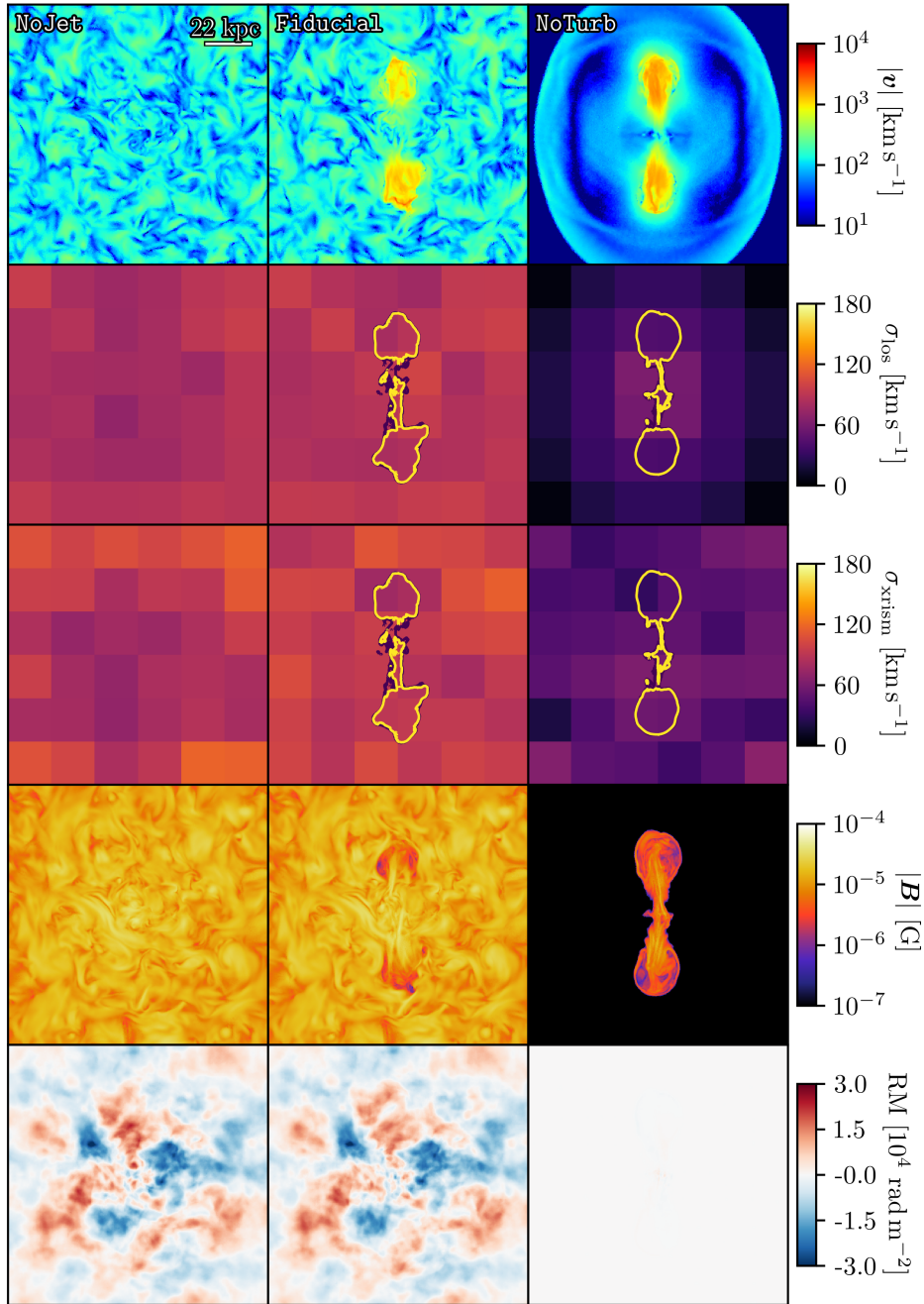


Figure 4. From left to right, we display simulations *NoJet*, *Fiducial* and *NoTurb* at 50 Myr. In the first row we show thin projections (4 kpc) of velocity $|v|$ weighted with density. The second row shows velocity dispersion estimates along the line of sight σ_{los} directly computed from the velocity distribution in the simulation. The third row depicts the velocity dispersion obtained from fits to mock spectra σ_{xrism} including instrumental effects of XRISM. The fourth row shows thin projections (4 kpc) of the magnetic field $|B|$ centred on the BH weighted with the volume. Finally, we show Faraday RM maps. Displayed images have dimensions $132 \text{ kpc} \times 132 \text{ kpc}$. Calculated velocity dispersion and RM encompass the full depth of the box (1.5 Mpc). Our initial turbulent magnetic field induces velocity dispersion at the observed level as seen for *NoJet* and *Fiducial*. The AGN affects turbulence (velocity dispersion) only in its near vicinity. Secondly, the contribution of the jet to RM is negligible.

turbulence, but rather turbulence induced by other processes such as fluctuations of the cluster potential as a result of mergers or accretion, substructure infall, or thermal instability (all of which are not included in these simulations). We discuss the required spatial resolution to detect the lobe-induced turbulence in the next subsection.

Although our analysis is limited to a single jet outburst, Fig-

ure 6 illustrates that jet-driven turbulence is spatially constrained to the wake of the rising bubbles. We focus on our model *NoTurb* and show the velocity dispersion of the ICM (top) and slices of the absolute velocity (bottom panels). The initial AGN outburst drives a shock wave into the ICM, which induces small-amplitude vorticity, which quickly decays. Significant turbulence is therefore limited to the wake region of the jet/bubbles, which is then advected upwards

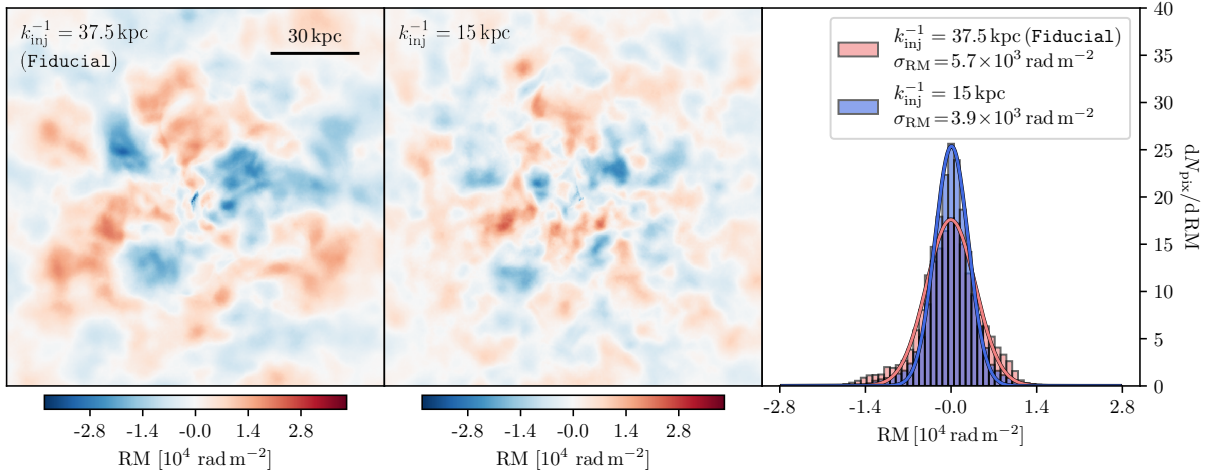


Figure 5. Maps of Faraday RM of our simulations with a magnetic injection scale $k_{\text{inj}}^{-1} = 37.5$ kpc (Fiducial model, left) and $k_{\text{inj}}^{-1} = 15$ kpc (centre). Histograms of RM distribution with corresponding dispersion σ_{RM} are shown on the right. A decreasing injection scale implies a smaller RM dispersion.

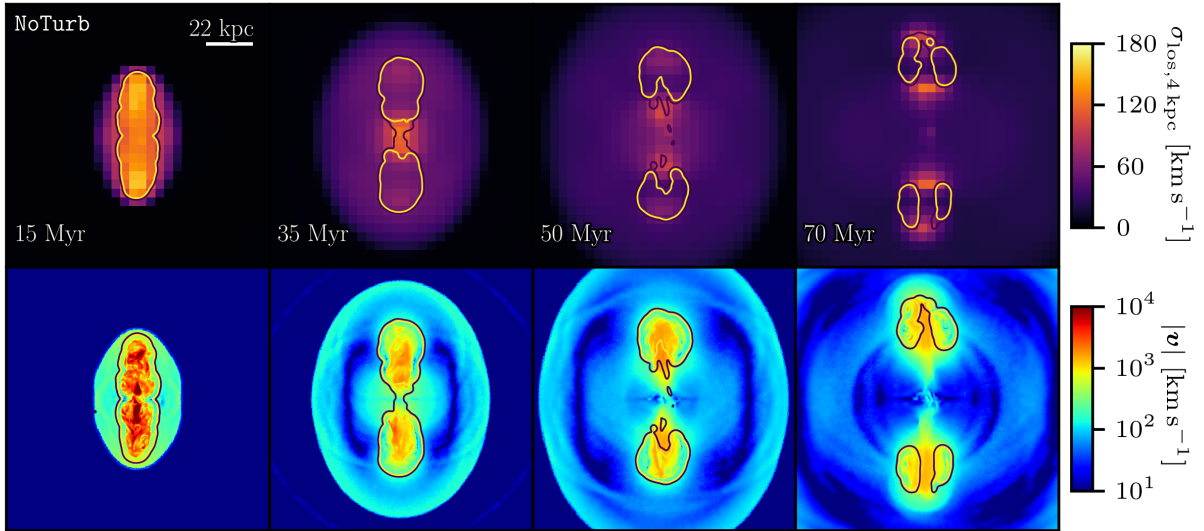


Figure 6. We show the velocity dispersion of the ICM (top) and slices of the velocity (bottom) at different times (left to right) of the model Noturb. We overlay contours of slices of the jet tracers $X_{\text{jet}} = \{10^{-3}, 10^{-2}\}$ (purple and yellow) to highlight the location of the lobes. Displayed images have dimensions $132 \text{ kpc} \times 132 \text{ kpc}$. After passing of the initial shock wave, the rising bubbles only causes an increased velocity field in the immediate wake of the bubbles.

as those buoyantly rise. Our jet parameters are modelled after detected bubbles in Perseus. While more powerful AGN events are expected to possess larger wake regions, they are not observed in Perseus. In addition, duty cycles are not observed in Perseus to be short enough for a concatenation of small outbursts to be able to sustain turbulence in the entire core region. Nevertheless, the uncertain degree of jet precession may potentially increase the level of isotropy of the jet driven turbulence somewhat.

Zhuravleva et al. (2014) infer the ICM heating rate due to dissipation of turbulence from X-ray observations of CC clusters. They conclude that the turbulent heating rate is sufficient to halt cooling in these clusters and suggest it as the main heating mechanism (Zhuravleva et al. 2016). In contrast, Mohapatra & Sharma (2019) find the required level of turbulence for turbulent dissipation to be the dominant heating mechanism to be inconsistent with *Hitomi* measurements. Our results indicate that lobes of the size of the ones in Perseus cannot be the sole driver for this level of turbulence.

This is in agreement with findings of other simulations in the literature (Reynolds et al. 2015; Bourne & Sijacki 2017; Bambic et al. 2018; Bambic & Reynolds 2019). Interestingly, simulations in self-regulated setups (e.g. Lau et al. 2017; Li et al. 2017) show slightly higher levels of turbulence.

4.3 Observational effects

In Figure 4 we show emission weighted velocity dispersion maps (second row) and velocity dispersion maps determined by fitting spectra of synthetic XRISM observations (third row). Overall, the two maps show agreement, highlighting the robustness of the method, however with a noteworthy systematically higher velocity dispersion in the outer regions of the synthetic observations. To understand this discrepancy, it is important to realize that the fitted line broadening is a superposition of thermal and Doppler broadening. Thus, to infer the velocity dispersion, we subtract the effect of

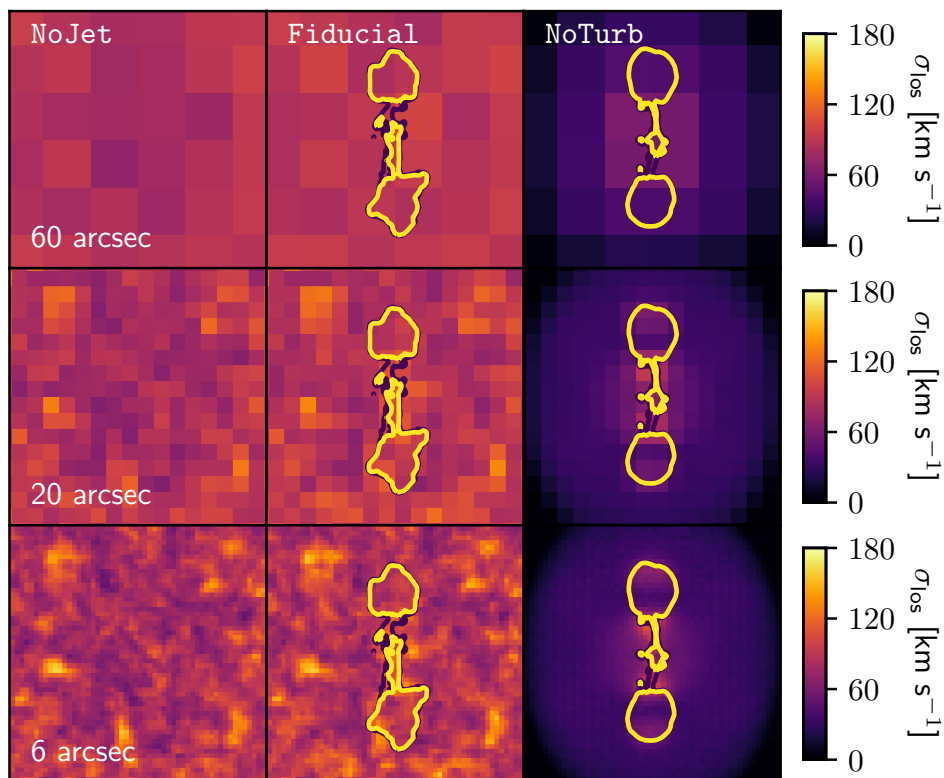


Figure 7. Emission weighted velocity dispersion maps with different spatial resolution.

thermal broadening, for which we assume a temperature of 4 keV. Since the cluster is set up as a cool-core cluster, its real temperature in the center is slightly lower in comparison to the edges of the projection, which leads to an incomplete subtraction of thermal broadening at the edges and thus an overestimate of the velocity dispersion in these regions. Note that the temperature differences in our simplified setup are likely lower than in reality since we do not include cooling or cosmological environment in our setup. In Appendix C we disentangle the instrumental effects from the effect of fitting the spectra on the inferred map.

In addition, we show emission weighted velocity dispersion maps at different spatial resolutions in Figure 7. While the 60 arcsec resolution map shows the overall level of velocity dispersion, the 20 arcsec resolution map already resolves the largest modes of the turbulence. Most strikingly on display at the highest resolution map (6 arcsec) is the fact that the *Fiducial* map seems to be a superposition of the external turbulence of the *NoJet* and the jet driven turbulence of the *NoTurb* runs. This indicates that the degree of ICM turbulence into which the jets are launched does not impact the extent to which they drive more turbulence. We speculate that this breaks down once the shape and position of the jet inflated lobes is substantially altered by existing ICM turbulence.

In summary, we find that the kinematic impact of the lobes is very localized, which is only identifiable at high resolution, when the lobes are spatially resolved. This is particularly true when considering the bulk velocities with superimposed lobe velocities seen at an inclination (not shown here). We note that we did not create full synthetic observations (in Figure 7) and ignored the effect of photon noise in this example. However, Figure 7 illustrates the wealth of additional information higher resolution velocity disper-

sion maps contain about the state of turbulence in the ICM and its origins.

We conclude that AGNs only drive turbulence locally. This is in line with previous work, which find AGNs to be very inefficient drivers of kinetic energy (Reynolds et al. 2015; Yang & Reynolds 2016; Bourne & Sijacki 2017; Hillel & Soker 2017a; Prasad et al. 2018). Consequently, cluster turbulence seen by Hitomi Collaboration (2016) appears rather related to sloshing motions initiated by mergers (ZuHone et al. 2018; Walker et al. 2018) and/or cosmological flows. Having shown that the main impact on gas flows from jets is in the wake of inflated lobes, we focus on this region in the following.

5 JET-INDUCED UPLIFT OF THE ICM

Cold gas is observed as disks and/or filamentary structures in the center of galaxy clusters (e.g., Koekemoer et al. 1999; Salomé et al. 2006; Russell et al. 2019). Submillimeter to optical observations reveal the complex velocity structures of cold gas. While disks show circular motions, filaments often surround bubbles or are found in the downstream regions. Predominantly smooth velocity gradients in filaments provide additional evidence that AGNs have a strong influence on their velocity structures (e.g., Werner et al. 2014; Tremblay et al. 2018; Gendron-Marsolais et al. 2018). Its origin is under debate. One idea is that cold gas condenses out of the hot phase when the ratio of cooling time t_{cool} and free-fall time t_{ff} fall below a critical value $t_{\text{cool}}/t_{\text{ff}} < 10$. This cold gas is then uplifted by an AGN (Gaspari et al. 2012; Voit et al. 2017). Alternatively, the thermal instability may be triggered by the turbulent uplift by an AGN (McNamara et al. 2016; Olivares et al. 2019; Martz et al. 2020) or possibly a sloshing galaxy (Vantyghem et al. 2019). Sim-

ulations by Beckmann et al. (2019) find evidence for the former two.

In the following, we focus on the flow patterns of gas that is dragged up by the jet from the vicinity of the SMBH. We employ our idealized, non-radiative MHD setup to separate motions induced by cooling from motions caused primarily by the AGN. Motions induced by condensating material that is collected in the so-called cloud-growth regime (Gronke & Oh 2018; Li et al. 2020; Sparre et al. 2020) require higher resolutions and are usually studied in dedicated simulations of cooling clouds submerged in hot winds. Consequently, this effect is not present in our setup.

Our analysis is focused on the `Fiducial` run at 50 Myr. In Figure 8, we portray the column density, velocity dispersion and mean velocity component along the line-of-sight of the traced gas in each row, respectively. The jet is rotated around the SMBH towards the observer (θ) and anti-clockwise in the plane (ϕ) at the same angle of $\theta = \phi = 0^\circ, 22^\circ, 45^\circ, 68^\circ$ in panels from left to right, respectively. At 50 Myr, lobes are inflated, which rise buoyantly as bubbles in the cluster. Their powerful wake causes magnetic field amplification and drags up gas from the center (Jones & De Young 2005; O’Neill et al. 2009). The later process is visible as filamentous structures of enhanced column densities that extend from the centre of the cluster to the bubbles.

Induced mean velocities are highest in the filamentous structures and exceed values of 1000 km s^{-1} . They are best visible when looking into the jet (high values of θ). Furthermore, the transverse component reaches velocities exceeding $\gtrsim 500 \text{ km s}^{-1}$. The inner material is dragged along with the jet while downwards motions towards the SMBH are more common in the outer parts of the cocoon. The dragged up material even penetrates the center of the bubble and the bubble morphs into a torus. High vorticity and turbulence is generated throughout the bubble and wake. However, the velocity dispersion of the dragged up material remains surprisingly low with velocities in the range $10 - 40 \text{ km s}^{-1}$.

Figure 9 shows a sample of four histograms that provide an overview of diversity seen in the velocity structure in individual pixels, corresponding to individual line-of-sight projections. Pixels show single Gaussian peaks with subdominant secondary flows (upper panels). At least two Gaussian components can be identified in the lower left panel. But we also find very heterogeneous velocity distributions in a significant fraction of pixels (lower right panel). Here, we see a clear peak in addition to many additional components moving in opposite directions. Thereby, a single Gaussian fit and its velocity dispersion cannot accurately account for the intermittent velocity structures of multiple velocity components in the flow patterns of the dragged-up material. Note that the turbulent ICM also influences the motion of the scalar. However, our comparison of induced velocities in `Fiducial` and `NoTurb` showed that the ICM contribution is secondary.

In summary, we are left with a remarkably coherent outflow in the wake of the bubble, at or exceeding the buoyant rising velocity of the jet-inflated bubble, reaching Mach numbers of almost unity (see Figure 6, bottom panel, sound speed around 10^3 km s^{-1}), and fairly insensitive to preexisting turbulence. Since the bubble velocity is mostly set by cluster properties and bubble size (Churazov et al. 2001), we expect it to be fairly insensitive to details of the jet other than the total injected energy (which determines the bubble size, as shown in Ehlert et al. 2018). In the outflow reference frame, the local velocity dispersions constitute Mach numbers of only around 0.01-0.05. This has important implications for future studies of the thermodynamics of these outflows since it allows to study thermal instability in local simulations of outward moving

patches of gas, without the need for a global, cluster wide simulation. While we only investigate one specific case, there is no reason to assume this changes qualitatively with changed jet parameters, though it is plausible to assume that the range of turbulent Mach numbers in the outflow frame across varying jet parameters is larger than presented here.

6 CONCLUSIONS

We run MHD simulations of jet-inflated bubbles in a Perseus-like CC cluster with a turbulent magnetic field. There is an inherent relation between large-scale magnetic and velocity fields, which we connect to two observables: line of sight velocity dispersion as measured by high spectral resolution X-ray spectroscopy and RM. Furthermore, we study the influence of the AGN on the velocity field, its detectability and the effect of spatial resolution. Finally, we analyze the velocity structure of uplifted central gas in the wake of the buoyantly rising radio-lobes. We summarize our findings as follows.

We find Faraday RMs that are an order of magnitude above observed values. This is somewhat surprising as magnetic field parameters were directly taken from observations. The magnetic field of the jet has negligible effect on the overall RM (see Section A). We identify four effects that could be responsible for the discrepancy. (i) Possibly our adopted coherence scale is too large and we therefore underpredict depolarization. To test this hypothesis, we ran an additional simulation with an injection scale of $k_{\text{inj}} = 15^{-1} \text{ kpc}^{-1}$, which decreases RM by 30% (see Figure 5). (ii) Observed RMs are limited to few small patches in clusters that are provided by the angular extends of radio lobes. Especially the bright central radio sources in CC clusters imply a large dynamic range that challenges high-frequency polarized observations of lobes, which are negligibly affected by Faraday depolarisation. (iii) Beam smoothing artificially lowers the dispersion of observed RMs. We neglect this effect here. (iv) Vazza et al. (2018) find their simulated magnetic fields to depart from a Gaussian distribution that is usually assumed when modeling Faraday RMs. Consequently, observations of RM possibly overestimate cluster magnetic field strengths. This highlights the relevance of cosmological MHD simulations that are able to self-consistently drive and sustain large scale magnetic fields. Moreover, this calls for a dedicated synthetic modeling of observations to take into account all possible observational effects.

- Measurements of large scale magnetic fields and velocities in galaxy clusters are inherently coupled. The strength, radial scaling and injection scale of our magnetic fields are motivated by observations. Interestingly, they yield RM values that are an order of magnitude higher than observed. However, observationally obtained magnetic field strengths may suffer from Faraday depolarization and only probe a very limited spatial window. Assuming too large magnetic coherence scales may also bias the inferred magnetic field strengths high. Finally, beam smoothing and possible departures from Gaussianity may further alleviate this discrepancy. Future work is needed to address this open problem.

- The influence of the AGN driven jet on the velocity fields is limited to the lobe’s proximity. Gas flows on scales larger than the characteristic size of the lobes are not AGN driven.

- Given the arcmin resolution of the analysis of the *Hitomi* data of Perseus, we conclude that the measured cluster turbulence is likely not directly driven by rising radio lobes.

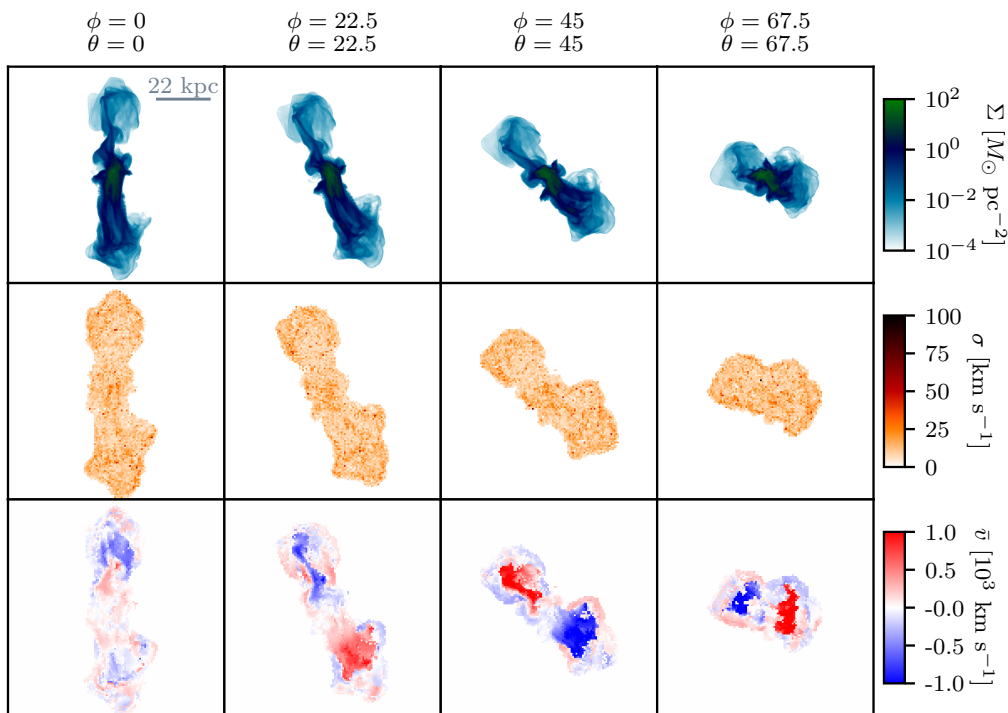


Figure 8. From top to bottom, we show surface density Σ of tracer material lifted from the center, tracer mass-weighted velocity dispersion σ and mean velocity \bar{v} along the line of sight through the simulation box. Variables are binned in pixels of $0.7 \text{ kpc} \times 0.7 \text{ kpc}$. Images have dimensions $90 \text{ kpc} \times 90 \text{ kpc}$. We show results for `Fiducial` at 50 Myr. From left to right, the jet is rotated towards the observer at angle θ and counter-clockwise in the plane at angle ϕ . The wake accelerates the tracers up to 1000 km s^{-1} along the jet axis (high θ). The main velocity component shows low dispersion. Our high resolution allows us good sampling of the velocity distribution.

- Central gas is dragged up in filament-like structures by the AGN. A complex multi-component velocity structure is induced in the lifted material. While the bulk velocity of the lifted material exceeds 1000 km s^{-1} , the line of sight velocity dispersion is remarkably low with only about 50 km s^{-1} . The previously central gas remains constrained to the wake and near proximity of the rising bubbles.

The connection of line of sight velocity dispersion and RM studied in this work highlights the multi-faceted nature of intra-cluster turbulence, and the role numerical simulations can play to connect the different observables. We restricted this study to non-radiative simulations in order to quantify the role of ‘stirring’ by rising radio lobes without the additional effects of an (AGN moderated) cooling flow, as well as to an individual outburst. In the future, we plan to study the influence of cooling on the local AGN-induced velocity fields. This will allow us to compare our model to observed filaments in CC clusters.

ACKNOWLEDGEMENTS

KE and RW would like to thank John ZuHone for the insightful discussions and for making the PYXSIM code publicly available. KE and CP acknowledge support by the European Research Council under ERC-CoG grant CRAGSMAN-646955.

DATA AVAILABILITY

The data underlying this article will be shared upon request to the corresponding author.

REFERENCES

- Asplund M., Grevesse N., Sauval A. J., Scott P., 2009, *Annu. Rev. Astron. Astrophys.*, 47, 481
- Bambic C. J., Reynolds C. S., 2019, *Astrophys. J.*, 886, 78
- Bambic C. J., Morsony B. J., Reynolds C. S., 2018, *Astrophys. J.*, 857, 84
- Beckmann R. S., et al., 2019, *Astron. Astrophys.*, 631, 1
- Beresnyak A., 2012, *Phys. Scr.*, 86, 058201
- Beresnyak A., Miniati F., 2016, *Astrophys. J.*, 817, 127
- Bîrzan L., Rafferty D. A., McNamara B. R., Wise M. W., Nulsen P. E. J., 2004, *Astrophys. J.*, 607, 800
- Bonafede A., Feretti L., Murgia M., Govoni F., Giovannini G., Dallacasa D., Dolag K., Taylor G. B., 2010, *Astron. Astrophys.*, 513, A30
- Bourne M. A., Sijacki D., 2017, *Mon. Not. R. Astron. Soc.*, 472, 4707
- Bourne A., Sijacki D., 2020, AGN jet feedback on a moving mesh: weak shocks and lobe disruption gently prevent the cooling catastrophe. preprint (arXiv:2008.12784) (arXiv:2008.12784v1)
- Bourne M. A., Sijacki D., Puchwein E., 2019, *Mon. Not. R. Astron. Soc.*, 490, 343
- Bulbul G. E., Smith R. K., Foster A., Cottam J., Loewenstein M., Mushotzky R., Shafer R., 2012, *Astrophys. J.*, 747, 32
- Chen Y.-H. H., Heinz S., Enßlin T. A., 2019, *Mon. Not. R. Astron. Soc.*, 11, 1939
- Cho J., 2014, *Astrophys. J.*, 797
- Churazov E., Brügggen M., Kaiser C. R., Böhringer H., Forman W., 2001, *Astrophys. J.*, 554, 261

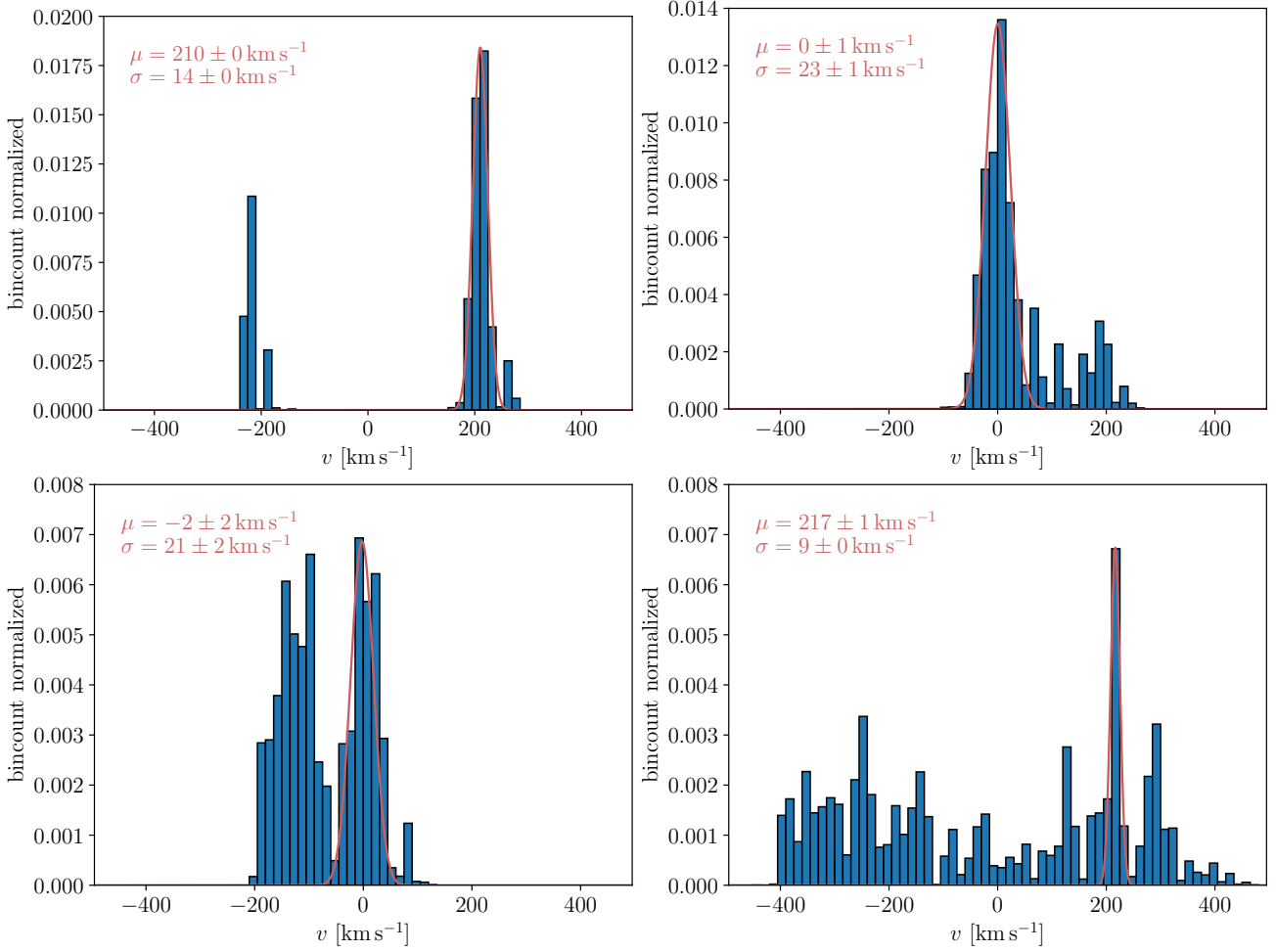


Figure 9. Histograms of the velocity of uplifted tracers by the AGN. Panels correspond to the line-of-sight velocity distribution in a single pixel weighted with tracer mass. We also overplot Gaussian fits that are used to determine mean velocity and velocity dispersion of the main velocity component (see Figure 8). The velocity distribution is dominated by a single Gaussian in the upper panels. However, the velocity distribution in the lower panels shows two distinct peaks or a predominantly flat distribution, respectively. The induced turbulent velocities show diverse and very complex distributions. Assuming a single velocity component is clearly insufficient to represent the complex flow structure.

Churazov E., Forman W., Jones C., Böhringer H., 2003, *Astrophys. J.*, 590, 225
 Churazov E., et al., 2012, *Mon. Not. R. Astron. Soc.*, 421, 1123
 Clarke T. E., 2004, *To Appear a Dedic. issue J. Korean Astron. Soc. (JKAS). Proc. "International Conf. Cosm. Rays Magn. Fields Large Scale Struct.*, p. 6
 De Plaa J., Zhuravleva I., Werner N., Kaastra J. S., Churazov E., Smith R. K., Raassen A. J., Grange Y. G., 2012, *Astron. Astrophys.*, 539, A34
 Diehl S., Li H., Fryer C. L., Rafferty D., 2008, *Astrophys. J.*, 687, 173
 Dolag K., Vazza F., Brunetti G., Tormen G., 2005, *Mon. Not. R. Astron. Soc.*, 364, 753
 Domínguez-Fernández P., Vazza F., Brüggén M., Brunetti G., 2019, *Mon. Not. R. Astron. Soc.*, 486, 623
 Donnert J., Dolag K., Lesch H., Müller E., 2009, *Mon. Not. R. Astron. Soc.*, 392, 1008
 Donnert J., Vazza F., Brüggén M., ZuHone J., 2018, *Space Sci. Rev.*, 214, 122
 Dubois Y., Devriendt J., Slyz A., Silk J., 2009, *Mon. Not. R. Astron. Soc. Lett.*, 399, 49
 Ehler K., Weinberger R., Pfrommer C., Pakmor R., Springel V., 2018, *Mon. Not. R. Astron. Soc.*, 481, 2878
 Enßlin T. A., Pfrommer C., Miniati F., Subramanian K., 2011, *Astron. Astrophys.*, 527, A99

Fabian A. C., 2012, *Annu. Rev. Astron. Astrophys.*, 50, 455
 Fabian A. C., Walker S. A., Russell H. R., Pinto C., Sanders J. S., Reynolds C. S., 2017, *Mon. Not. R. Astron. Soc.*, 464, L1
 Fujita Y., Cen R., Zhuravleva I., 2020, *Mon. Not. R. Astron. Soc.*, 494, 5507
 Gaspari M., Churazov E., 2013, *Astron. Astrophys.*, 559
 Gaspari M., Ruszkowski M., Sharma P., 2012, *Astrophys. J.*, 746, 94
 Gendron-Marsolais M., et al., 2018, *Mon. Not. R. Astron. Soc.*, 479, L28
 Gitti M., Brighenti F., McNamara B. R., 2012, *Adv. Astron.*, 2012
 Govoni F., et al., 2010, *Astron. Astrophys.*, 522, 1
 Govoni F., et al., 2017, *Astron. Astrophys.*, 603, A122
 Gronke M., Oh S. P., 2018, *Mon. Not. R. Astron. Soc.*, 480, L111
 Gu L., Zhuravleva I., Churazov E., Paerels F., Kaastra J., Yamaguchi H., 2018, *Space Sci. Rev.*, 214
 Guidetti D., Murgia M., Govoni F., Parma P., Gregorini L., de Ruiter H., Cameron R. A., Fanti R., 2008, *Astron. Astrophys.*, 483, 699
 Guidetti D., Laing R. A., Croston J. H., Bridle A. H., Parma P., 2012, *Mon. Not. R. Astron. Soc.*, 423, 1335
 Guo F., Oh S. P., 2008, *Mon. Not. R. Astron. Soc.*, 384, 251
 Guo F., Duan X., Yuan Y. F., 2018, *Mon. Not. R. Astron. Soc.*, 473, 1332
 Han J., 2017, *Annu. Rev. Astron. Astrophys.*, 55, 111
 Hillel S., Soker N., 2017a, *Mon. Not. R. Astron. Soc. Lett.*, 466, L39
 Hillel S., Soker N., 2017b, *Astrophys. J.*, 845, 91
 Hillel S., Soker N., 2018, *Res. Astron. Astrophys.*, 18, 81

- Hitomi Collaboration 2016, *Nature*, 535, 117
- Hitomi Collaboration 2018, *Publ. Astron. Soc. Japan*, 70, 9
- Jacob S., Pfrommer C., 2017a, *Mon. Not. R. Astron. Soc.*, 467, 1449
- Jacob S., Pfrommer C., 2017b, *Mon. Not. R. Astron. Soc.*, 467, 1478
- Jones T. W., De Young D. S., 2005, *Astrophys. J.*, 624, 586
- Kazantsev A., 1968, *Sov. J. Exp. Theor. Phys.*, 26, 1031
- Koekemoer A. M., O’Dea C. P., Sarazin C. L., McNamara B. R., Donahue M., Voit G. M., Baum S. A., Gallimore J. F., 1999, *ApJ*, 525, 621
- Kuchar P., Enßlin T. A., 2011, *Astron. Astrophys.*, 529, 13
- Kulsrud R. M., 2005, *Plasma Physics for Astrophysics*. Princeton University Press, Princeton, NJ
- Lau E. T., Gaspari M., Nagai D., Coppi P., 2017, *Astrophys. J.*, 849, 54
- Li Y., Ruszkowski M., Bryan G. L., 2017, *Astrophys. J.*, 847, 106
- Li Z., Hopkins P. F., Squire J., Hummels C., 2020, *Mon. Not. R. Astron. Soc.*, 492, 1841
- Loewenstein M., Zweibel E. G., Begelman M. C., 1991, *Astrophys. J.*, 377, 392
- Martizzi D., Quataert E., Faucher-Giguère C. A., Fielding D., 2019, *Mon. Not. R. Astron. Soc.*, 483, 2465
- Martz C. G., et al., 2020, *Astrophys. J.*, 897, 57
- McNamara B. R., Nulsen P. E. J., 2012, *New J. Phys.*, 14, 40
- McNamara B. R., Russell H. R., Nulsen P. E. J., Hogan M. T., Fabian A. C., Pulido F., Edge A. C., 2016, *Astrophys. J.*, 830, 1
- Mohapatra R., Sharma P., 2019, *Mon. Not. R. Astron. Soc.*, 484, 4881
- Mukherjee D., Bicknell G. V., Sutherland R., Wagner A., 2016, *Mon. Not. R. Astron. Soc.*, 461, 967
- Mukherjee D., Bodo G., Mignone A., Rossi P., Vaidya B., 2020, *Mon. Not. R. Astron. Soc.*, 499, 681
- Navarro J. F., Frenk C. S., White S. D. M., 1996, *ApJ*, 462, 563
- Navarro J. F., Frenk C. S., White S. D. M., 1997, *ApJ*, 490, 493
- O’Neill S. M., De Young D. S., Jones T. W., 2009, *Astrophys. J.*, 694, 1317
- Ogorzalek A., et al., 2017, *Mon. Not. R. Astron. Soc.*, 472, 1659
- Olivares V., et al., 2019, *Astron. Astrophys.*, 631, A22
- Ota N., Yoshida H., 2016, *Publ. Astron. Soc. Japan*, 68, S19
- Ota N., et al., 2007, *Prog. Theor. Phys. Suppl.*, 59, S351
- Pakmor R., Springel V., Bauer A., Mocz P., Munoz D. J., Ohlmann S. T., Schaal K., Zhu C., 2016a, *Mon. Not. R. Astron. Soc.*, 455, 1134
- Pakmor R., Pfrommer C., Simpson C. M., Kannan R., Springel V., 2016b, *Mon. Not. R. Astron. Soc.*, 462, 2603
- Pfrommer C., 2013, *Astrophys. J.*, 779, 10
- Pfrommer C., Pakmor R., Schaal K., Simpson C. M., Springel V., 2017, *Mon. Not. R. Astron. Soc.*, 465, 4500
- Pinto C., et al., 2015, *Astron. Astrophys.*, 575, A38
- Prasad D., Sharma P., Babul A., 2018, *Astrophys. J.*, 863, 62
- Rafferty D. A., McNamara B. R., Nulsen P. E. J., Wise M. W., 2006, *Astrophys. J.*, 652, 216
- Reiprich T. H., Bohringer H., 2002, *Astrophys. J.*, 567, 716
- Reynolds C. S., Balbus S. A., Schekochihin A. A., 2015, *Astrophys. J.*, 815, 41
- Roh S., Ryu D., Kang H., Ha S., Jang H., 2019, *Astrophys. J.*, 883, 138
- Rudnick L., Blundell K. M., 2003, *Astrophys. J.*, 588, 143
- Russell H. R., et al., 2019, *Mon. Not. R. Astron. Soc.*, 490, 3025
- Ruszkowski M., Yang H. Y. K., Reynolds C. S., 2017, *Astrophys. J.*, 844, 13
- Ryu D., Kang H., Cho J., Das S., 2008, *Science (80-.)*, 320, 909
- Salomé P., et al., 2006, *Astron. Astrophys.*, 454, 437
- Sanders J. S., Fabian A. C., 2013, *Mon. Not. R. Astron. Soc.*, 429, 2727
- Sanders J. S., Fabian A. C., Smith R. K., Peterson J. R., 2010, *Mon. Not. R. Astron. Soc. Lett.*, 402, L11
- Schekochihin A. A., Cowley S. C., 2006, *Phys. Plasmas*, 13
- Schober J., Schleicher D. R., Federrath C., Bovino S., Klessen R. S., 2015, *Phys. Rev. E - Stat. Nonlinear, Soft Matter Phys.*, 92, 023010
- Schuecker P., Finoguenov A., Miniati F., Bohringer H., Briel U. G., 2004, *Astron. Astrophys.*, 426, 387
- Sharma P., Chandran B. D. G., Quataert E., Parrish I. J., 2009, *ApJ*, 699, 348
- Simionescu A., et al., 2019, *Space Sci. Rev.*, 215
- Smith R. K., Brickhouse N. S., Liedahl D. A., Raymond J. C., 2001, *Astrophys. J.*, 556, L91
- Sparre M., Pfrommer C., Ehlert K., 2020, *Mon. Not. R. Astron. Soc.*, 4281, 4261
- Springel V., 2010, *Mon. Not. R. Astron. Soc.*, 401, 791
- Subramanian K., 1999, *Phys. Rev. Lett.*, 83, 15
- Sugawara C., Takizawa M., Nakazawa K., 2009, *Publ. Astron. Soc. Japan*, 61, 1293
- Tamura T., Hayashida K., Ueda S., Nagai M., 2011, *Publ. Astron. Soc. Japan*, 63, S1009
- Tamura T., et al., 2014, *Astrophys. J.*, 782, 38
- Tang X., Churazov E., 2017, *Mon. Not. R. Astron. Soc.*, 468, 3516
- Tchekhovskoy A., Bromberg O., 2016, *Mon. Not. R. Astron. Soc.*, 461, L46
- Thomas T., Pfrommer C., 2019, *Mon. Not. R. Astron. Soc.*, 485, 2977
- Thomas T., Pfrommer C., Enßlin T., 2020, *Astrophys. J. Lett.*, 890, L18
- Tremblay G. R., et al., 2018, *Astrophys. J.*, 865, 13
- Vacca V., Murgia M., Govoni F., Feretti L., Giovannini G., Perley R. A., Taylor G. B., 2012, *Astron. Astrophys.*, 540, A38
- Vacca V., Murgia M., Govoni F., Enßlin T., Oppermann N., Feretti L., Giovannini G., Loi F., 2018, *Galaxies*, 6, 1
- Vantyghem A. N., et al., 2019, *Astrophys. J.*, 870, 57
- Vazza F., Brunetti G., Brüggén M., Bonafede A., 2018, *Mon. Not. R. Astron. Soc.*, 474, 1672
- Vogt C., Enßlin T. A., 2005, *Astron. Astrophys.*, 434, 67
- Voit G. M., Meece G., Li Y., Shea B. W. O., Bryan G. L., Donahue M., 2017, *Astrophys. J.*, 845, 80
- Walker S. A., Sanders J. S., Fabian A. C., 2015, *Mon. Not. R. Astron. Soc.*, 453, 3699
- Walker S. A., Sanders J. S., Fabian A. C., 2018, *Mon. Not. R. Astron. Soc.*, 481, 1718
- Weinberger R., Ehlert K., Pfrommer C., Pakmor R., Springel V., 2017, *Mon. Not. R. Astron. Soc.*, 470, 4530
- Werner N., Zhuravleva I., Churazov E., Simionescu A., Allen S. W., Forman W., Jones C., Kaastra J. S., 2009, *Mon. Not. R. Astron. Soc.*, 398, 23
- Werner N., et al., 2014, *Mon. Not. R. Astron. Soc.*, 439, 2291
- Wiener J., Pfrommer C., Peng Oh S., 2017, *Mon. Not. R. Astron. Soc.*, 467, 906
- Wilms J., Allen A., McCray R., 2000, *Astrophys. J.*, 542, 914
- Xu H., et al., 2002, *Astrophys. J.*, 579, 600
- Xu H., Li H., Collins D. C., Li S., Norman M. L., 2009, *Astrophys. J.*, 698, L14
- Yang H.-Y. K., Reynolds C. S., 2016, *Astrophys. J.*, 829, 90
- Yuan F., Gan Z., Narayan R., Sadowski A., Bu D., Bai X.-n., 2015, *Astrophys. J.*, 804, 101
- Zhuravleva I., et al., 2014, *Nature*, 515, 85
- Zhuravleva I., et al., 2016, *Mon. Not. R. Astron. Soc.*, 458, 2902
- Zhuravleva I., Allen S. W., Mantz A., Werner N., 2018, *Astrophys. J.*, 865, 53
- ZuHone J. A., Hallman E. J., 2016, *Astrophys. Source Code Libr.*
- ZuHone J., Miller E. D., Bulbul E., Zhuravleva I., 2018, *Astrophys. J.*, 853, 180
- Zweibel E. G., 2013, *Phys. Plasmas*, 20, 055501
- de Gasperin F., et al., 2012, *Astron. Astrophys.*, 547, A56
- van Weeren R. J., de Gasperin F., Akamatsu H., Brüggén M., Feretti L., Kang H., Stroe A., Zandanel F., 2019, *Space Sci. Rev.*, 215

APPENDIX A: VARYING MAGNETIC FIELD PARAMETERS

We varied the initial magnetic field strength in our simulations and depict the resulting velocity dispersion in Figure A1. The magnetic-to-thermal pressure ratio in the ICM $X_{B,ICM}$ decreases as $X_{B,ICM} = 0.25, 0.05, 0.01$ from left to right. Consequently, the velocity dispersion decreases as $\gtrsim 150 \text{ km s}^{-1}$, $\sim 100 \text{ km s}^{-1}$ and $\lesssim 60 \text{ km s}^{-1}$, respectively. The lowest magnetic field run $\times 1$

cannot stir the ICM sufficiently, to reach the velocity dispersion observed by *Hitomi*. Both X25 and X5 produce a velocity dispersion that is consistent with *Hitomi* measurements. However, we emphasize that cosmological simulations are necessary to follow the evolution of the magnetic dynamo and obtain self-consistent velocity fields.

In addition, we show simulations at decreasing resolution from left to right in Figure A2. The velocity dispersion decreases slightly with resolution. This is likely due to the increased numerical diffusivity in the lower resolution runs, which decrease the effectiveness of the stirring on longer timescales. The RMs show higher maxima in the low resolution run. Intermittent magnetic field strengths are less resolved so that the cancelling of RM is reduced.

Turning our attention now to the influence of jet magnetic fields on the overall RM, we see that RM is dominated by the contributions from the ICM. In Figure A3 we compare the total RM from ICM and jet (left) with the RM from the jet only (right). Some rims of the bubble and sparse filaments show relatively high signal. Here, only a few cells exceed the threshold in X_{jet} and thereby suffer from minimal depolarization. Comparing magnitudes, we see that the lobes contribute at least two orders of magnitude less signal compared to the ICM. This is consistent with observations, that would otherwise generally suffer from considerable beam polarization (e.g., Han 2017). Note however, that some sources show evidence for a dominating contribution from locally compressed ICM close to the lobes (Rudnick & Blundell 2003; Guidetti et al. 2012).

APPENDIX B: JET RESOLUTION STUDY

To improve the numerical convergence with respect to the distance traveled of our jets, we introduce an opening angle δ_j to the model. As discussed in Section 2.2, half of the momentum is injected with an angle smaller than 10 degree from the jet axis, while the maximum angle is 30 degree. While the jet initially fans out, it is almost immediately collimated by the pressure of the ambient ICM. This leads to an overall broadening of the jet where better resolved jets are affected more. Thereby better convergence of jet distance is obtained. In Figure B1, we contrast the bubble distance with and without opening angle as a function of time for simulations at three different resolutions. Simulations with an opening angle of $\delta_j = 30^\circ$ converge more to similar distances than those without opening angle ($\delta_j = 0^\circ$).

APPENDIX C: SYNTHETIC X-RAY OBSERVATIONS

Figure C1 shows velocity dispersion maps using different methods from a full synthetic observation (top row), a fit to photon spectrum, i.e. synthetic observation without instrument response (middle row), and a 2 – 12 keV emission weighted velocity dispersion. While there is a systematic increase in velocity dispersion originating from a higher temperatures at the outskirts of the projection, the instrumental effect mainly introduces scatter on a pixel by pixel basis.

This paper has been typeset from a $\text{\TeX}/\text{\LaTeX}$ file prepared by the author.

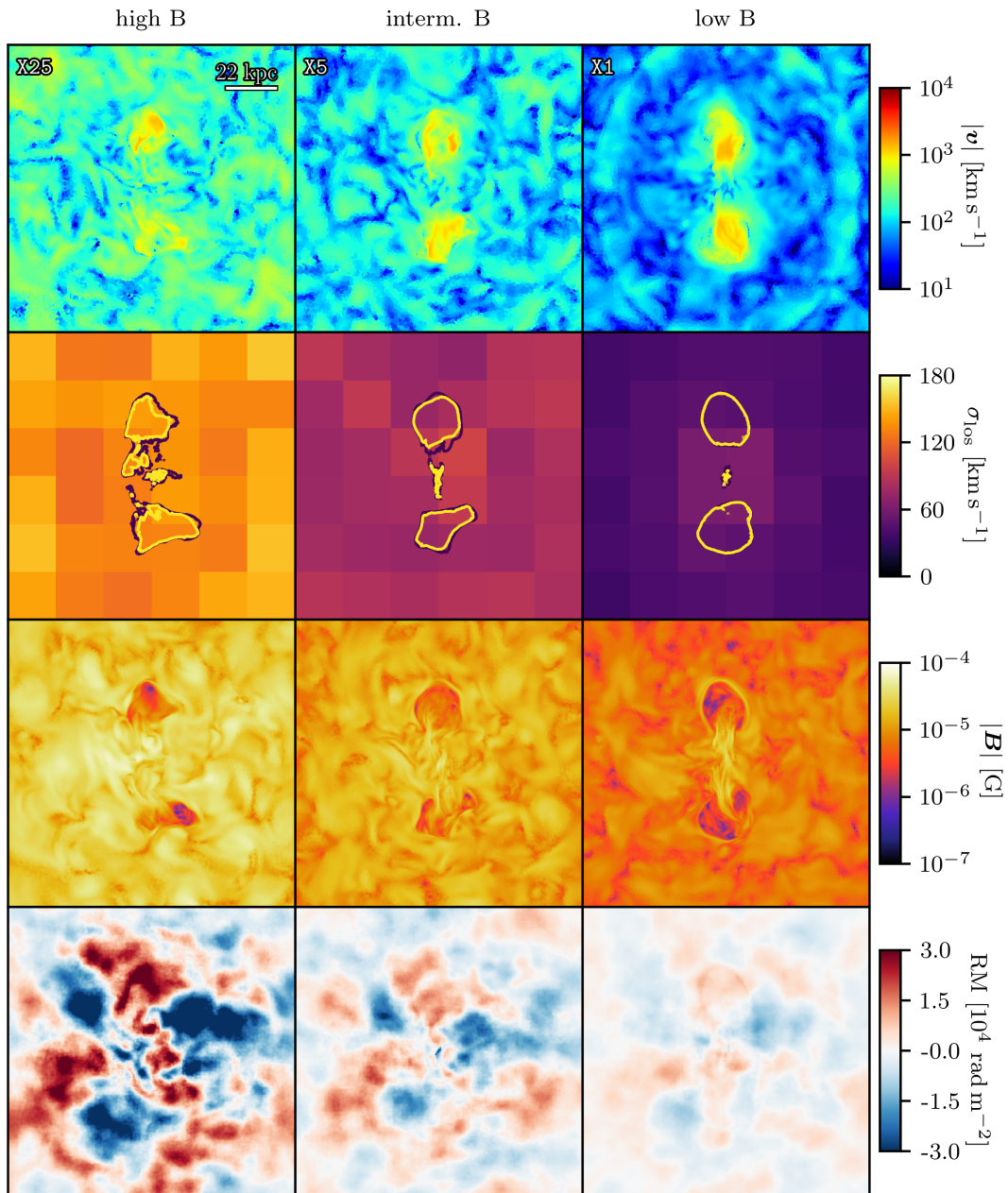


Figure A1. From left to right, we compare runs X25, X5, X1 with varying magnetic field strengths $X_B = 0.25, 0.05, 0.01$, respectively. A higher magnetic field strength provides a stronger tension force that induces higher velocities and velocity dispersion in the ICM. Both X25 and X5 induce a velocity dispersion consistent with *Hitomi* measurements, X25 is at the upper end and X5 thereby preferred. See Figure 4 for details on shown quantities.

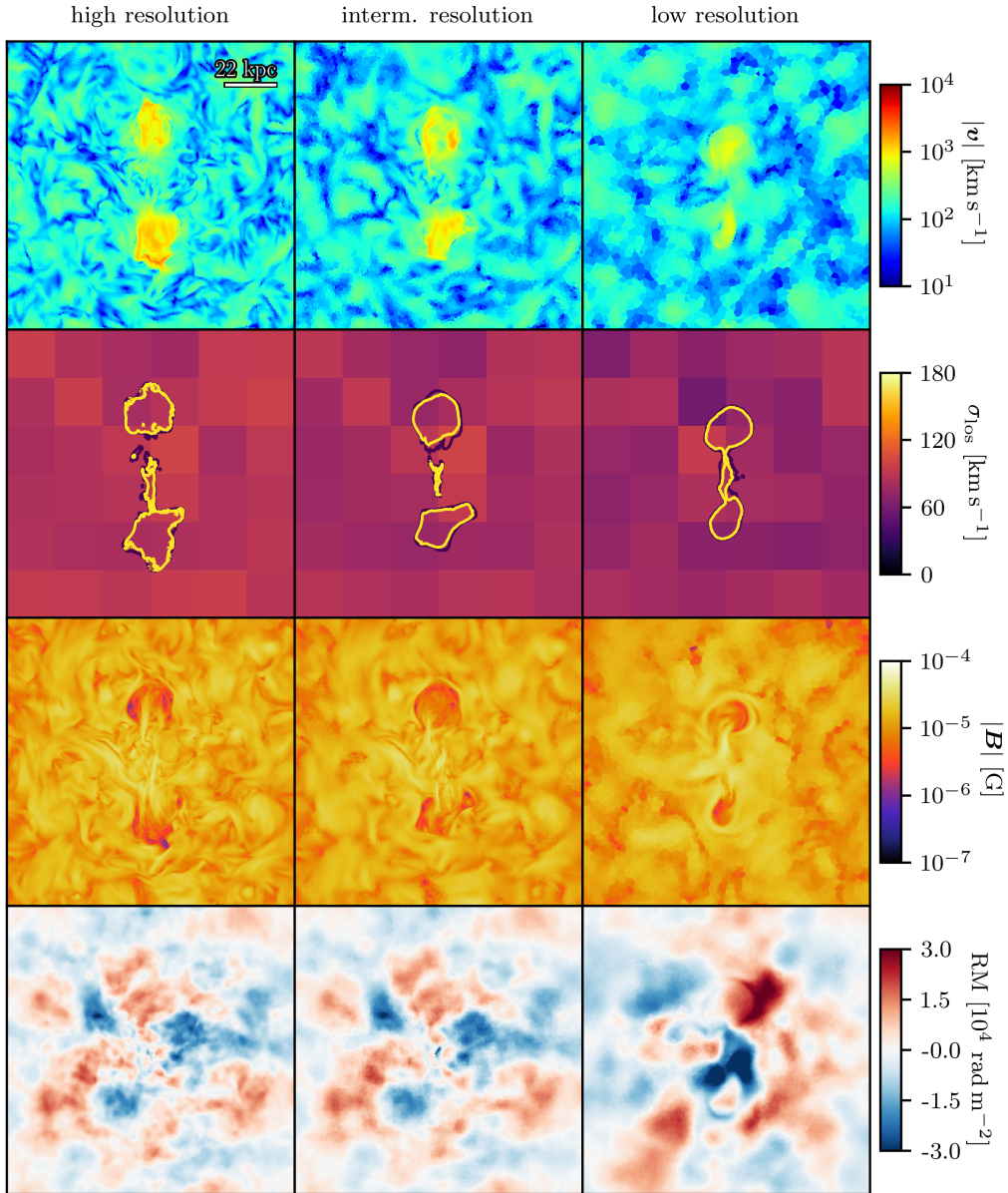


Figure A2. From left to right, we compare simulations at high, intermediate and low resolution, respectively. The loss of small scale structures leads to an increase in RM for the low resolution run as depolarization is reduced. However, overall features in runs at high and intermediate resolution show convergence. See Figure 4 for details on shown quantities.

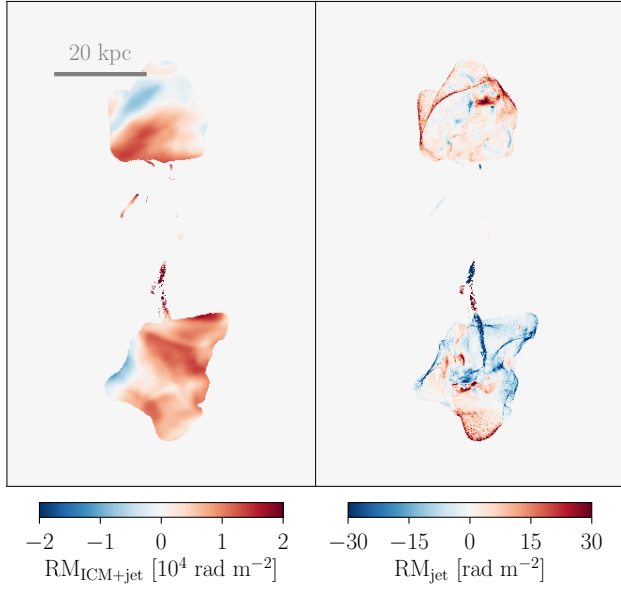


Figure A3. We show the RM of the fiducial run at 50 Myr for varying sources of emission. On the left, we include both the ICM and AGN as the source. On the right, we show the contribution from jet only ($X_{\text{jet}} > 10^{-3}$). The ICM contribution dominates the RM signal by at least two orders of magnitude. The enhancement in parts of the bubbles' rim and some filaments is an artifact of the tagging process of the lobes.

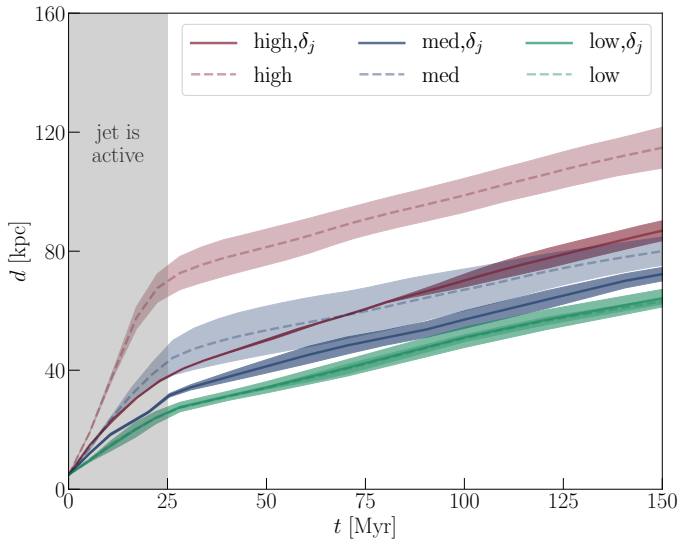


Figure B1. Average distance of the jets at low, intermediate and high resolution (shown with different colours) as a function of time. We compare our new model that includes an opening angle of $\delta_j = 30^\circ$ (solid lines) to simulations with our previous model ($\delta_j = 0^\circ$, dashed lines). The errorbars indicate the distance of the individual jets. Including an opening angle leads to improved numerical convergence of the jet distance travelled, especially for jets at high resolution.

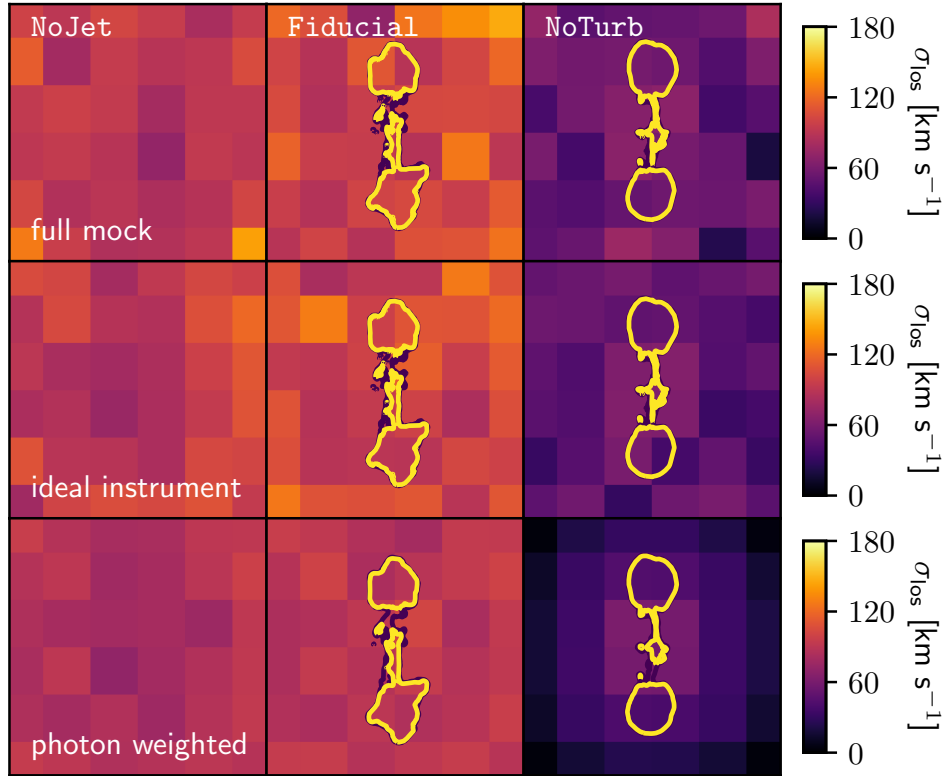


Figure C1. Velocity dispersion maps from mock Xrism observations (top), fits to the emitted photon spectrum (center) and the emission weighted velocity dispersion (bottom).